

Evaluation of candidate models for the 13th generation International Geomagnetic Reference Field

Patrick Alken

Cooperative Institute for Research in Environmental Sciences

Erwan Thebault (✉ erwan.thebault@univ-nantes.fr)

Université de Nantes <https://orcid.org/0000-0002-7038-2855>

Ciaran Beggan

British Geological Survey

Julien Aubert

Université de Paris, Institut de Physique du Globe de Paris

Julien Baerenzung

University of Potsdam

William J. Brown

British Geological Survey

S. Califf

Cooperative Institute for Research in Environmental Sciences

Arnaud Chulliat

Cooperative Institute for Research in Environmental Sciences

G.A. Cox

British Geological Survey

Christopher C. Finlay

DTU Space, Technical University of Denmark

Alexandre Fournier

Université de Paris, Institut de Physique du Globe de Paris

Nicolas Gillet

"Université Grenoble Alpes"

Magnus D. Hammer

DTU Space, Technical University of Denmark

Matthias Holschneider

University of Potsdam

Gauthier Hulot

Université de Paris, Institut de Physique du Globe de Paris

Monika Korte

Deutsches Geoforschungszentrum Potsdam

Vincent Lesur

Université de Paris, Institut de Physique du Globe de Paris

Philippe W. Livermore

School of Earth and Environment, University of Leeds

Frank J. Lowes

University of Newcastle

Susan Macmillan

British Geological Survey - Edinburgh Office

Manoj Nair

Cooperative Institute for Research in Environmental Sciences

Nils Olsen

DTU Space, Technical University of Denmark

G. Ropp

Université de Paris, Institut de Physique du Globe de Paris

Martin Rother

Deutsches Geoforschungszentrum Potsdam

Neesha Schnepf

Cooperative Institute for Research in Environmental Sciences

Claudia Stolle

Deutsches Geoforschungszentrum Potsdam

Hiroaki Toh

Kyoto University

Fotini Vervelidou

Deutsches Geoforschungszentrum Potsdam

Pierre Vigneron

Université de Paris, Institut de Physique du Globe de Paris

Ingo Wardinski

Universität de Strasbourg, Institut de Physique du Globe de Strasbourg

Technical report

Keywords: IGRF, magnetic field modeling, geomagnetism

Posted Date: September 9th, 2020

DOI: <https://doi.org/10.21203/rs.3.rs-41022/v2>

License:  This work is licensed under a Creative Commons Attribution 4.0 International License.

[Read Full License](#)

Version of Record: A version of this preprint was published on February 11th, 2021. See the published version at <https://doi.org/10.1186/s40623-020-01281-4>.

RESEARCH

Evaluation of candidate models for the 13th generation International Geomagnetic Reference Field

P. Alken^{1,2*}, E. Thébault³, C. D. Beggan⁴, J. Aubert⁶, J. Baerenzung¹³, W. J. Brown⁴, S. Califf^{1,2}, A. Chulliat^{1,2}, G. A. Cox⁴, C. C. Finlay⁵, A. Fournier⁶, N. Gillet⁷, M. D. Hammer⁵, M. Holschneider¹³, G. Hulot⁶, M. Korte¹⁰, V. Lesur⁶, P. W. Livermore⁸, F. J. Lowes⁹, S. Macmillan⁴, M. Nair^{1,2}, N. Olsen⁵, G. Ropp⁶, M. Rother¹⁰, N. R. Schnepf^{1,2}, C. Stolle¹⁰, H. Toh¹¹, F. Vervelidou¹⁰, P. Vigneron⁶ and I. Wardinski¹²

Abstract

In December 2019, the 13th revision of the International Geomagnetic Reference Field (IGRF) was released by the International Association of Geomagnetism and Aeronomy (IAGA) Division V Working Group V-MOD. This revision comprises two new spherical harmonic main field models for epochs 2015.0 (DGRF-2015) and 2020.0 (IGRF-2020) and a model of the predicted secular variation for the interval 2020.0 to 2025.0 (SV-2020-2025). The models were produced from candidates submitted by fifteen international teams. These teams were led by the British Geological Survey (UK), China Earthquake Administration (China), Universidad Complutense de Madrid (Spain), University of Colorado Boulder (USA), Technical University of Denmark (Denmark), GFZ German Research Centre for Geosciences (Germany), Institut de physique du globe de Paris (France), Institut des Sciences de la Terre (France), Pushkov Institute of Terrestrial Magnetism, Ionosphere and Radio Wave Propagation (Russia), Kyoto University (Japan), University of Leeds (UK), Max Planck Institute for Solar System Research (Germany), NASA Goddard Space Flight Center (USA), University of Potsdam (Germany), and Université de Strasbourg (France). The candidate models were evaluated individually and compared to all other candidates as well to the mean, median and a robust Huber-weighted model of all candidates. These analyses were used to identify, for example, the variation between the Gauss coefficients or the geographical regions where the candidate models strongly differed. The majority of candidates were sufficiently close that the differences can be explained primarily by individual modeling methodologies and data selection strategies. None of the candidates were so different [as](#) to warrant their exclusion from the final IGRF-13. The IAGA V-MOD task force thus voted for two approaches: the median of the Gauss coefficients of the candidates for the DGRF-2015 and IGRF-2020 models and the robust Huber-weighted model for the predictive SV-2020-2025. In this paper, we document the evaluation of the candidate models and provide details of the approach used to derive the final IGRF-13 products. [We also perform a retrospective analysis of the IGRF-12 SV candidates over their performance period \(2015-2020\). Our findings suggest that forecasting secular variation can benefit from combining physics-based core modeling with satellite observations.](#)

Keywords: IGRF, magnetic field modeling, geomagnetism

1 Introduction

2 The International Geomagnetic Reference Field (IGRF) is a series of models describing the large-scale in-
3 ternal part of Earth's magnetic field. The spherical harmonic coefficients comprising the IGRF are agreed
4 upon by an international task force of geomagnetic field modeling experts and are typically updated every
5 five years to account for temporal field variations originating in Earth's core. The task force overseeing
6 IGRF operates under the auspices of the International Association of Geomagnetism and Aeronomy (IAGA)
7 Working Group V-MOD. The IGRF model is used by academia, government, and industry in a wide va-
8 riety of applications including magnetic reference systems, long-term dynamics of the Earth's core field,
9 ionospheric electrodynamics, space weather phenomena, electromagnetic induction, local magnetic anoma-
10 lies in the Earth's crust, surveying, and orientation in three dimensions. Readers interested in the history
11 of IGRF are referred to [Barton \(1997\)](#) and [Macmillan and Finlay \(2011\)](#). The purpose of this paper is to
12 summarize all of the candidate models which were submitted for consideration for the thirteenth generation
13 of IGRF (hereafter IGRF-13) and to report the methods used by the task force to evaluate the candidates
14 and construct the final IGRF-13 models.

15 The IGRF-13 task force was formally elected at an IAGA V-MOD Working Group business meeting in
16 Cape Town on 28 August 2017, however several additional members joined afterward. The full IGRF-13 task
17 force consists of the authors of this paper. On 26 March 2019, the task force issued an international call for
18 modeling teams to contribute candidates for (1) a new Definitive Geomagnetic Reference Field (DGRF) for
19 epoch 2015.0 to spherical harmonic (SH) degree and order 13, (2) a new provisional IGRF for epoch 2020.0
20 to SH degree and order 13, and (3) a predictive constant secular variation (SV) forecast for the interval
21 2020.0 to 2025.0 to SH degree and order 8. The term 'definitive' is used because the best available datasets
22 before and after the epoch were used by the modeling teams, and so any further substantial improvement of
23 these retrospectively determined models is unlikely. In contrast, the provisional IGRF model will eventually
24 be replaced by a definitive model in a future revision of the IGRF when the community has a more complete
25 knowledge of the Earth's magnetic field for epoch 2020.0.

26 A record eleven candidate models were received for DGRF-2015, twelve for IGRF-2020, and fourteen for
27 the 2020-2025 SV forecast. In total, fifteen international teams participated in the IGRF-13 call. During
28 the fall of 2019, the task force evaluated each candidate model using well-established methodologies. The
29 task force voted on the procedure to determine the final IGRF-13 models based on the recommendations
30 of each evaluation report. Each institution participating in the task force received one vote for each of the
31 three models under consideration. The task force released IGRF-13 on 19 December 2019. The official set of

32 spherical harmonic coefficients as well as a discussion of the general features of the IGRF-13 model can be
33 found in [Alken et al \(2020b\)](#).

34 The fifteen teams who participated in the IGRF-13 call were led by the British Geological Survey (UK),
35 China Earthquake Administration (China), Universidad Complutense de Madrid (Spain), University of Col-
36 orado Boulder (USA), Technical University of Denmark (Denmark), GFZ German Research Centre for
37 Geosciences (Germany), Institut de physique du globe de Paris (France), Institut des Sciences de la Terre
38 (France), Pushkov Institute of Terrestrial Magnetism, Ionosphere and Radio Wave Propagation (Russia),
39 Kyoto University (Japan), University of Leeds (UK), Max Planck Institute for Solar System Research (Ger-
40 many), NASA Goddard Space Flight Center (USA), University of Potsdam (Germany), and Université de
41 Strasbourg (France). See Table 1 for a list of models submitted by each team as well as references to pa-
42 pers describing the preparation of each candidate model in detail. The table also lists the letter codes used
43 throughout this paper to refer to specific candidate models for the different teams.

44 The number of institutions who participated in the IGRF-13 is larger than for any previous generation,
45 which highlights the advance of global capability in this area of research. The composition of the teams shows
46 strong cooperation between scientists both within their own countries and internationally. Geomagnetic field
47 modeling is reliant on the high-quality data collected by the various space agencies and institutes which
48 operate satellites and ground-based observatories. In addition to satellite data, modelers made extensive use
49 of data from the international network of ground geomagnetic observatories either directly, or indirectly in
50 the form of magnetic indices monitoring the level of magnetic activities.

51 The IGRF-13 candidate models were built primarily using data recorded by the European Space Agency
52 (ESA) Swarm satellite mission (2013-present) and ground magnetic observatories. One team used the China
53 Earthquake Administration's CSES mission ([Shen et al, 2018](#)) exclusively for its candidate model ([Yang
54 et al, 2020](#)). Some teams built parent models spanning longer time intervals, which additionally made use of
55 data from the CHAMP (2000-2010), Ørsted (1999-2013), and SAC-C (2000-2004) missions. Additionally, one
56 team used data recorded by the ESA Cryosat-2 mission (2010-present) to supplement the ground observatory
57 network during the gap period between CHAMP and Swarm ([Finlay et al, 2020](#)).

58 The definition of the internal field as requested by IGRF-13 has some ambiguity. In previous generations, it
59 was considered to include the core field, long wavelength lithospheric field, steady oceanic and tidal magnetic
60 fields and induced fields due to time-varying external sources. During past IGRF generations, some teams
61 attempted to separate the effects of the induced field, arguing that it was not truly an internal field. However,
62 a counter argument made at the IAGA 2017 DIV-V business meeting suggested it remains extremely difficult,
63 at present, to effectively remove the internally induced ionospheric field in a consistent manner, as there is
64 insufficient resolution of Earth's global conductivity. In addition, many IGRF users require knowledge of the

65 combined field due to all internal sources on or above Earth's surface. This led to the general agreement at
66 the meeting that the induced field and tidal fields should remain within the IGRF main field model to avoid
67 introducing a step into the Gauss coefficients between generations.

68 As in previous generations, a variety of data selection, processing, and modeling procedures have been
69 used to build the IGRF-13 candidates. We briefly summarize the approaches of the various groups below;
70 the detailed descriptions of the techniques used to derive the individual candidate models can be found in
71 the papers appearing in this special issue (see Table 1).

72 For the main field at epochs 2015.0 and 2020.0, some teams derived their candidate models from parent
73 models describing the magnetic field over multi-decadal periods by combining datasets from several satel-
74 lite missions and ground observatories (Finlay *et al.*, 2020; Huder *et al.*, 2020; Ropp *et al.*, 2020; Sabaka
75 *et al.*, 2020; Wardinski *et al.*, 2020). Several teams built parent models covering the full Swarm satellite mis-
76 sion era (November 2013 to present) (Brown *et al.*, 2020; Rother *et al.*, 2020; Vigneron *et al.*, 2020). Other
77 teams built dedicated main field candidate models for each of the epochs requested by the call, thus us-
78 ing data within smaller time windows centered on 2015.0, or immediately preceding 2020.0 (Alken *et al.*,
79 2020a; Pavón-Carrasco *et al.*, 2020; Petrov and Bondar, 2020; Yang *et al.*, 2020), which required less complex
80 parameterization in time. Some teams co-estimated a low-degree external field model representing magneto-
81 spheric sources (Brown *et al.*, 2020; Finlay *et al.*, 2020; Huder *et al.*, 2020; Pavón-Carrasco *et al.*, 2020; Ropp
82 *et al.*, 2020; Rother *et al.*, 2020; Sabaka *et al.*, 2020; Vigneron *et al.*, 2020; Yang *et al.*, 2020). Two teams co-
83 estimated additional geomagnetic source fields in their parent models (Ropp *et al.*, 2020; Sabaka *et al.*, 2020).
84 For DGRF-2015, the teams simply output snapshot Gauss coefficients from their parent models at 2015.0
85 truncated to degree 13. For IGRF-2020, extrapolation of the Gauss coefficients to 2020.0 was required, as the
86 candidate models were delivered to the task force in October 2019. Many teams used linear or spline-based
87 extrapolation of their parent model Gauss coefficients to accomplish this.

88 For the predictive secular variation models covering 2020.0 to 2025.0, the candidates broadly fall into two
89 main categories: (1) computing SV solely from the latest available satellite and ground data (Alken *et al.*,
90 2020a; Finlay *et al.*, 2020; Huder *et al.*, 2020; Pavón-Carrasco *et al.*, 2020; Petrov and Bondar, 2020; Rother
91 *et al.*, 2020), or (2) applying physics-based modeling, combined with recent satellite and ground data to
92 forecast future field changes based on underlying core dynamics (Brown *et al.*, 2020; Fournier *et al.*, 2020;
93 Metman *et al.*, 2020; Minami *et al.*, 2020; Sanchez *et al.*, 2020; Tangborn *et al.*, 2020; Wardinski *et al.*, 2020).
94 Accurately forecasting the temporal evolution of the main geomagnetic field is nontrivial, due to challenges
95 such as the low resolution of the recoverable magnetic field at the core-mantle boundary, the occurrence of
96 unpredictable geomagnetic jerks or the uncertainty associated with diffusion of the field over short timescales
97 (e.g. Bärenzung *et al.*, 2018; Maus *et al.*, 2008a; Whaler and Beggan, 2015). As an example, in the past two

98 decades, the northern polar region has experienced large variations with the location of the magnetic dip
99 pole moving in an irregular manner (Alken *et al.*, 2020b; Chulliat *et al.*, 2010; Livermore *et al.*, 2020; Thébault
100 *et al.*, 2015). In the section [Retrospective analysis of IGRF-12 secular variation models](#), we examine the
101 performance of the IGRF-12 SV forecasts over the 2015-2020 time interval to investigate how physics-based
102 approaches compare to the empirical SV derived from recent satellite data.

103 Members of the volunteer task force carried out evaluations of the candidate models submitted by the
104 different teams. Assessment of the candidate models was primarily based on statistical criteria. Some main
105 field (MF) and SV models showed greater consistency than others. However, close statistical agreement
106 between models does not necessarily mean that these models are ‘correct’. It can also be a consequence
107 of using similar data selection or modeling techniques. For this reason, the evaluation of the task force
108 members also relied on companion descriptions of the candidate models as well as on their expert opinion,
109 and in certain cases, comparisons with independent data sets.

110 To decide the mechanism for deriving the final models, the task force chair (P. Alken) prepared a ballot
111 with all suggestions put forth by the individual evaluation teams. The vote was held in December 2019,
112 and the task force chose to select the median of the Gauss coefficients of all candidates for the DGRF-
113 2015 and IGRF-2020 main field models, and an iterative robust weighting in space for the SV-2020-2025
114 model (see [Robust Huber model](#)). The resulting IGRF-13 coefficients were prepared and checked before
115 being made available to the public through the IAGA Division V, V-MOD working group web page ([http:
116 //www.ngdc.noaa.gov/IAGA/vmod/igrf.html](http://www.ngdc.noaa.gov/IAGA/vmod/igrf.html)). Updated software, web services and online calculators are
117 also available for public use (see Alken *et al.* (2020b, Sec. 5)).

118 The next section of this paper summarizes the statistical criteria used by the task force members for the
119 testing and the inter-comparison of the candidate models. We then discuss the procedure used to build a
120 robust Huber-weighted model, followed by analyses of all candidates for the DGRF-2015, IGRF-2020 and
121 SV-2020-2025. Next we provide a retrospective analysis of the IGRF-12 secular variation forecasts over
122 2015.0-2020.0. Finally, we provide details of the final adoption of the IGRF-13 models.

123 **Evaluation methodology**

The IGRF is a series of mathematical models describing the internal geomagnetic field on and above Earth’s
surface, and a prediction of its annual rate of change (known as secular variation) for five years beyond the
date of issue. We assume there are no local magnetic field sources in the IGRF region of validity, so that the
global magnetic field can be expressed as the gradient of a scalar potential, $\mathbf{B} = -\nabla V$. The scalar potential

V is approximated as a finite series,

$$V(r, \theta, \phi, t) = a \sum_{n=1}^N \sum_{m=0}^n \left(\frac{a}{r}\right)^{n+1} [g_n^m(t) \cos(m\phi) + h_n^m(t) \sin(m\phi)] P_n^m(\cos \theta) \quad (1)$$

124 Here, $g_n^m(t)$ and $h_n^m(t)$ are the Gauss coefficients which depend on time t , conventionally given in units of
 125 nanoTesla (nT). The coordinates (r, θ, ϕ) are geocentric radius, co-latitude, and longitude, and $a = 6371.2$ km
 126 is a reference value approximating the mean Earth radius. The functions P_n^m are the Schmidt semi-normalized
 127 associated Legendre functions of degree n and order m (Winch *et al.*, 2005). N specifies the spherical harmonic
 128 degree truncation value, which was chosen to be 10 up to and including epoch 1995, after which it was
 129 increased to 13 to model smaller scale internal signals which can be captured by high-resolution satellite
 130 missions such as Ørsted, CHAMP and Swarm.

131 The IGRF-13 teams submitted sets of Gauss coefficients g_n^m, h_n^m to SH degree and order 13 for DGRF-2015
 132 and IGRF-2020 in units of nT, and first time derivatives \dot{g}_n^m, \dot{h}_n^m to SH degree and order 8 for SV-2020-
 133 2025 in units of nT/year. In the evaluation of the candidates, we compared two models by computing
 134 differences of the Gauss coefficients and plotting spatial difference maps of the field components. Past IGRF
 135 evaluations found it prudent to also compare individual candidates with the mean and median models of all
 136 candidates, and the IGRF-13 task force continued this practice. We also calculated a robust Huber iteratively
 137 reweighted model in space from all candidate models following the procedure used for IGRF-12 (see [Robust](#)
 138 [Huber model](#)).

139 In the sections below, we briefly define the statistics which were used to evaluate the IGRF-13 candidate
 140 models. These same quantities were used during the IGRF-11 (Finlay *et al.*, 2010) and IGRF-12 (Thébault
 141 *et al.*, 2015) evaluations. In the equations which follow, we use the main field Gauss coefficients g_n^m, h_n^m for
 142 convenience, however the secular variation coefficients \dot{g}_n^m, \dot{h}_n^m may be substituted in their place in order to
 143 analyze the SV candidate models.

144 Model Differences

We examine differences between two models in order to identify regions of strong discrepancies, both in the
 spatial and spectral domains. Because the Gauss coefficients in the scalar potential (Eq. (1)) appear as linear
 terms, we can compute direct differences of these parameters from two different models, and substitute the
 differences into the relevant equations, both for the scalar potential V and vector geomagnetic field \mathbf{B} . If we
 define the Gauss coefficients of a particular candidate model i by ${}_i g_n^m$ and ${}_i h_n^m$, then the coefficient difference

between two models i and j is defined as

$$\begin{aligned} {}_{i,j}g_n^m &= {}_i g_n^m - {}_j g_n^m \\ {}_{i,j}h_n^m &= {}_i h_n^m - {}_j h_n^m \end{aligned} \quad (2)$$

145 Since coefficients at higher degrees are far smaller in magnitude than the lower degrees, we will consider
146 weighted differences $\sqrt{n+1} |{}_{i,j}g_n^m|$ and $\sqrt{n+1} |{}_{i,j}h_n^m|$ when plotting these quantities in this paper.

147 Spherical Harmonic Power Spectral Differences

The mean square value of the vector geomagnetic field over a sphere of radius r due to all harmonics of SH degree n for a given candidate model i is (Lowes, 1966, 1974)

$${}_i R_n(r) = (n+1) \left(\frac{a}{r}\right)^{2n+4} \sum_{m=0}^n [({}_i g_n^m)^2 + ({}_i h_n^m)^2] \quad (3)$$

This is known as the Lowes-Mauersberger power spectrum, and may also be applied to the differences between two models,

$${}_{i,j} R_n(r) = (n+1) \left(\frac{a}{r}\right)^{2n+4} \sum_{m=0}^n [({}_{i,j} g_n^m)^2 + ({}_{i,j} h_n^m)^2] \quad (4)$$

Summing the power ${}_{i,j} R_n$ over all SH degrees from 1 to the truncation level N and then taking the square root provides the root mean square (rms) vector field difference between models i and j ,

$${}_{i,j} T(r) = \sqrt{\sum_{n=1}^N {}_{i,j} R_n(r)} \quad (5)$$

148 In this paper, we will use the notation ${}_i R_n$, ${}_{i,j} R_n$, and ${}_{i,j} T$ to denote these quantities computed at the Earth
149 mean radius $r = a$.

150 Azimuthal Power Spectral Differences

The Lowes-Mauersberger expression in Eq. (3) organizes spectral power in terms of spherical harmonic degree n . It is also instructive to analyze power as a function of the azimuthal ratio $az = m/n$, which varies from 0 for zonal harmonics to 1 for sectoral harmonics. We define the ratio as positive for the g_n^m coefficients and negative for the h_n^m . The azimuthal power is then defined as the mean square value of the field over a sphere of radius r produced by all harmonics with the same azimuthal ratio. For model i , the azimuthal power spectrum is defined as

$${}_i R_{az}(r) = \sum_{(m,n) \in A_{az}} (n+1) \left(\frac{a}{r}\right)^{2n+4} [({}_i g_n^m)^2 + ({}_i h_n^m)^2] \quad (6)$$

where $A_{az} = \{(m, n) \in \mathbb{Z}^2 : m/n = az\}$. In this paper we will primarily compute spectral differences between two models i and j ,

$${}_{i,j}R_{az}(r) = \sum_{(m,n) \in A_{az}} (n+1) \left(\frac{a}{r}\right)^{2n+4} [({}_{i,j}g_n^m)^2 + ({}_{i,j}h_n^m)^2] \quad (7)$$

151 In this paper, we calculate the azimuthal power for each ratio m/n , and bin the results in 29 bins of width
 152 $1/(N+1)$. The values in each bin are then summed together to obtain the power in that bin. Note, we will
 153 use the notation ${}_{i,j}R_{az}$ to denote azimuthal power at the Earth's mean radius $r = a$.

154 Degree Correlation

At $r = a$, the correlation per degree between two models i and j is defined as (Langel and Hinze, 1998, pg. 81)

$${}_{i,j}\rho_n = \frac{\sum_{m=0}^n ({}_{i,j}g_n^m {}_{i,j}g_n^m + {}_{i,j}h_n^m {}_{i,j}h_n^m)}{\sqrt{(\sum_{m=0}^n [({}_{i,j}g_n^m)^2 + ({}_{i,j}h_n^m)^2]) (\sum_{m=0}^n [({}_{j,i}g_n^m)^2 + ({}_{j,i}h_n^m)^2])}} \quad (8)$$

155 In this paper, we will primarily compute the degree correlation between a candidate model i and a reference
 156 model, such as the mean or median of all candidates, in which case the ${}_{j,i}g_n^m, {}_{j,i}h_n^m$ coefficients would be
 157 replaced with the Gauss coefficients of the reference model in Eq. (8). This can provide guidance on whether
 158 the harmonics of a given candidate correlate poorly with the reference model at particular degrees.

159 Robust Huber model

To build the robust Huber model, the Gauss coefficients of each candidate model were used to compute the vector geomagnetic field components at the Earth's mean radius on an equal area grid with 10000 nodes (Leopardi, 2006). On each grid node, there are as many vector field values as candidate models. The variations among candidates at each node produce an ensemble of magnetic field values. The Huber algorithm in space iteratively reweights the geomagnetic vector components of each candidate on the grid according to its deviation from the ensemble of available candidate model predictions. This produces Huber weights for the candidate model at each node in the three vector field components. The weights range from 0 to 1, illustrating regions where the candidate models agree (or disagree) with the ensemble of magnetic field predictions. This numerical computation is based on the Huber error distribution (Huber, 1981)

$$H(\epsilon) = \frac{1}{N_c} \begin{cases} \exp(-\epsilon^2/2), & |\epsilon| < c \\ \exp(-c|\epsilon| + c/2), & |\epsilon| \geq c \end{cases} \quad (9)$$

160 where N_c is the number of available candidate models. The parameter ϵ is the residual between the N_c
 161 candidate models vector values and the maximum likelihood model estimated in the least-squares sense,

162 normalized by a robust estimate of the residual standard deviation. The constant c is chosen as a compromise
 163 between a Laplace distribution (obtained when $c = 0$) and a Gaussian distribution (obtained when $c \rightarrow \infty$).
 164 Our Huber weighting scheme uses $c = 1.5$.

165 All N_c vector field values on the nodes of the grid are thus associated with their Huber weights. The final
 166 model is the inversion of the Huber-weighted gridded magnetic vector field values from each candidate in
 167 spherical harmonics (see Thébaud *et al* (2015) for further details). The major advantage of this method is
 168 that all candidates are considered: even if some disagree in certain regions, they provide an input to the final
 169 model. The Gauss coefficients of the median, mean and Huber-weighted models are provided on the IAGA
 170 website (https://www.ngdc.noaa.gov/IAGA/vmod/IGRF13/Mean_Median_Models/).

171 Evaluation of candidate models

172 Analysis of DGRF-2015 candidate models

173 The call for the DGRF-2015 requested models describing the large-scale internal field up to SH degree 13 with
 174 Gauss coefficients defined to a precision of 0.01 nT. We list the eleven candidate models (and their references)
 175 received for epoch 2015.0 in Table 1. All DGRF-2015 candidate models used vector fluxgate magnetometer
 176 (VFM) Swarm measurements as their primary data source, with the exception of the IP model, which used
 177 measurements from the absolute scalar magnetometer (ASM) instrument on Swarm (Vigneron *et al*, 2020).
 178 The ASM instrument is capable of providing both scalar and vector measurements (Fratter *et al*, 2016; Léger
 179 *et al*, 2015).

180 In Table 2, we present the rms vector field differences ($_{i,j}T$ in nT) between the individual candidate models
 181 i and j at the Earth's reference radius $r = a$. The last three columns show the rms difference between each
 182 candidate model i and (a) the simple arithmetic mean model M , (b) the median model M_{med} and (c) the
 183 robust Huber-weighted model. The required precision of 0.01 nT corresponds to a rounding error of just
 184 0.13 nT. All models show rms differences well above this value illustrating the nuances from the various data
 185 selection and field modeling approaches adopted by each team.

186 From Table 2, we observe that candidates B, CM, CU, D, G, IP, N, and P are in closer agreement with
 187 the arithmetic mean and median models than models IS, IZ, and S. The rms difference between each model
 188 of this first group and the mean/median models is less than 5 nT. The bottom row of Table 2 gives the
 189 arithmetic means of the rms vector field differences of $_{i,j}T$ of model i from the other models j . Again, models
 190 B, CM, CU, D, G, IP, N, and P have the smaller mean differences. Model IS is the most distinct with a
 191 mean rms difference to all models of 8.89 nT.

192 The median and robust models in Table 2 have the smallest average difference from the candidates (3.37
 193 and 3.33 nT). The difference between these two values is small, and since, as will be discussed later, we

194 have selected the median model as the final DGRF-2015, we use the median model as the reference in the
 195 following comparisons. Figure 1 (left) shows the spectral difference per degree (${}_{i,j}R_n$) between the candidate
 196 models and the median model. We find that the degree 1 and 2 coefficients of the IS model deviate most
 197 from the median, while degree 5 of the IZ model exhibits the largest difference. The right panel illustrates
 198 the degree correlation between the candidates and the median model, which is over 0.999 for all candidates
 199 up to SH degree 10. The absolute differences of Gauss coefficients (weighted by a factor $\sqrt{n+1}$) between
 200 the candidates and the median model coefficients are small, with the majority below 0.5 nT. Figure 2 (left)
 201 illustrates the values for each coefficient. The azimuthal power spectrum is shown in the right panel.

202 We present in Figure 3 the differences between the candidate models and the median model for the vertical
 203 (B_z) component at $r = a$. Some candidates show zonal structure (CM, IZ) or hemispherical differences
 204 (N) while the IS model suggests some secular variation is not accounted for due to the pattern of strong
 205 small-scale structures in the Indian Ocean regions and large-scale structure over North and South America,
 206 reminiscent of SV maps. The maps show there is little difference between the robust Huber model and the
 207 median model at $r = a$.

208 For the DGRF model candidates, it is possible to compare their magnetic field predictions directly to
 209 Swarm satellite data around 1 January 2015. We compared each candidate to one month of vector and scalar
 210 data from Swarm A and Swarm B (15 December 2014 to 15 January 2015). The Swarm data were sub-
 211 sampled to a rate of 1 sample every 15 seconds with local times between 21:00 and 05:00. We additionally
 212 selected geomagnetically quiet data with $K_p < 2$ and $|dRC/dt| \leq 4$ nT/hour. Finally, we removed the MF7
 213 lithospheric field model (Maus *et al.*, 2008b) and the CHAOS-6 external field model (Finlay *et al.*, 2016; Olsen
 214 *et al.*, 2014) from the Swarm data. A total of 21113 measurements were available for the comparison. The
 215 vector and scalar residuals between the Swarm measurements and each DGRF-2015 candidate model were
 216 computed. The statistics of the residuals equatorward of $\pm 55^\circ$ quasi-dipole latitude are presented in Table 3.
 217 The mean, median and robust models explain the Swarm measurements as well or better than many of
 218 the individual candidates. Figure 4 shows the residuals of the vertical component (B_z , North-East-Center
 219 (NEC) frame) between the Swarm data and DGRF-2015 candidate models. We see several models have
 220 larger residuals over the South Atlantic Anomaly region, which we attribute to the larger secular variation
 221 of B_z seen in this region, even over the one month period under consideration. The IS model has relatively
 222 large B_z residuals in this region, which is likely related to the treatment of their SV as seen in Fig. 3. Many
 223 of the maps display north-south along-track oscillations. These are primarily due to the SH degrees 14 and
 224 15 which were not removed from the Swarm data, as the DGRF models are truncated at degree 13, while
 225 the MF7 crustal field starts at degree 16.

226 Analysis of IGRF-2020 candidate models

227 We performed a similar analysis for the twelve candidate models submitted to IGRF for epoch 2020.0. Because
228 magnetic field measurements were not available close to the desired epoch of 1 January 2020, the derivation
229 of the main field candidates for the IGRF-2020 model was more challenging than for DGRF-2015. Many
230 teams utilized satellite and ground data up to mid-2019 for their model calculations and then extrapolated
231 the main field to 2020.0. Eleven of the candidates are based on Swarm Level 1b data and many include
232 ground-based observatory data. The CE model is based solely on data from the Chinese Seismology and
233 Electromagnetism Satellite (Shen *et al.*, 2018), which collected high latitude data specifically for IGRF-13.
234 Most candidates use relatively simple forms of extrapolation (e.g. linear or spline) from the end-point of their
235 model in 2019 to extend their main field to 1 January 2020. As shown in Table 4, the various extrapolation
236 schemes resulted in larger rms vector field differences between the IGRF-2020 candidates compared to the
237 DGRF-2015 candidates.

238 The rms differences vary from around 5 to 15 nT with no obvious clustering of models. There is a reasonably
239 uniform distribution of the differences, which suggests there is no ‘best’ population of models. However, the
240 CE, G, and S candidates differ the most from the rest of the population with consistently higher differences
241 compared to other candidates. The bottom row of the table is the arithmetic mean of the columns, and can
242 be considered as an average difference of a given candidate model with respect to all other candidates.

243 The mean, median and robust models have the lowest average differences from the candidate models, with
244 the median and robust models showing similar values (7.81 vs 7.78 nT). We again choose the median model
245 as the reference for comparison, since this is the model which was chosen for the final IGRF-2020 as will be
246 discussed later. Figure 5 (left) shows the power spectral difference per degree between the candidates and
247 the median model (note the logarithmic scale of the y-axis). There is a wider variation in the mean square
248 differences per degree for the IGRF-2020 candidates (up to 70 nT² compared to 15 nT² for the DGRF-2015
249 candidates). The CE model differs in degree 2, G in the degrees 3, 4 and 5, IZ mostly in degree 2, and S in
250 degrees 1 and 3. As shown in the right panel of Fig. 5, the degree correlation remains above 0.99 until degree
251 11 for all candidates.

252 Figure 6 (left) plots the absolute differences between the candidate Gauss coefficients and their median,
253 weighted by a factor of $\sqrt{n+1}$. The individual coefficients have larger differences in general compared to
254 the DGRF-2015. In the right panel, the azimuthal power spectrum indicates stronger differences for $m = n$
255 for the G model. Most models have an increase in the spectral difference for the zonal terms. This is most
256 likely due to contributions from the magnetospheric ring current and its Earth-induced part, despite efforts
257 to minimize this effect.

Figure 7 shows the differences in the vertical component between the IGRF-2020 candidate models and the median at 2020.0. Many of the maps exhibit north-south hemispherical differences with respect to the median model, which arise from the variations in the $n = 1$ dipole terms among the candidate models. The maps also show the effects of the extrapolation to 2020.0 as the scale bar is now ± 50 nT (c.f. ± 20 nT for Figure 3). Similar patterns are visible such as the zonal and auroral differences in the CM candidate and the SV-related differences in the IS candidate. Some models have an obvious sectoral or hemispherical difference, such as B, CU, N and P. The CE candidate shows generally positive differences in the mid-latitudes and negative variation at the auroral zones. The G candidate has large differences in the western hemisphere and central Pacific Ocean.

Analysis of IGRF-13 SV-2020-2025 candidate models

Fourteen teams submitted candidate models for the predicted secular variation in the 2020.0-2025.0 time period. For these models, teams submitted model coefficients \dot{g}_n^m, \dot{h}_n^m to spherical harmonic degree and order 8, which represent the average annual change in the Gauss coefficients between 2020.0-2025.0 in units of nT/year. The institutes which led the different SV candidate models are presented in Table 1.

There are a variety of approaches for forecasting secular variation. The B candidate uses core flow modeling with steady flow and acceleration, while CU, D and G use extrapolation of measured secular variation from the previous year or longer. The CM candidate made predictions in a similar manner, but produced it from an ensemble of field models built with a bootstrap approach from subsets of observations. The IP, K, P, M and N candidates use assimilation of ground and/or satellite data with geodynamo model outputs to form an estimate of secular variation. IS uses an ensemble of models from a stochastic prior and predicts with a Best Linear Unbiased Estimator. The L candidate used core flow combined with magnetic diffusion for its forecast. The S model has employed a singular spectral analysis of sixty years of SV to provide candidate values while IZ produced a spectral fit to each individual Gauss coefficient.

The candidates offer a diverse set of approaches to compute SV over the period 2020.0 to 2025.0 which produces a wide variation between the candidates, as seen in Table 5. The candidate differences fall into two fairly distinct categories – those that match each other to within 15 nT/yr and those whose differences are greater than 20 nT/yr. The candidates most different from the rest of the population are N, S, and K.

From visual inspection of the Gauss coefficients, it is noted that the K candidate has a small dipole (\dot{g}_1^0) SV coefficient of 1.9 nT/yr compared to 6–7 nT/yr for most of the other models. The S model has a negative \dot{g}_1^0 coefficient of -6.4 nT/yr as well as a high \dot{g}_1^1 coefficient of 11.5 nT/yr compared to 7–8 nT/yr in others. These coefficients contribute predominantly to the differences between these two and the other candidates.

289 Finally, the N model has significantly different degree 2 zonal coefficients compared to the other candidates
290 and thus shows strong variation.

291 The mean, median and robust models computed from the candidates have an average difference of around
292 11 nT/yr (last three columns of Table 5). When computing the Huber-weighted model, candidates CM, K,
293 and S showed large-scale differences with respect to the ensemble of candidates that are down-weighted by
294 the Huber weighting scheme. Model IZ is moderately down-weighted. The spatial difference between the
295 robust model and the median model remains below 5 nT/yr everywhere on the $r = a$ reference surface. The
296 robust model has a slightly smaller overall difference to the candidates (10.84 vs 10.92 nT/yr).

297 Figure 8 (left) shows the wide variation of the candidates in terms of their power spectral differences with
298 the robust model. The S model has the strongest degree 1 difference, while the K and N models have large
299 degree 2 variations. The degree correlation of the models is much lower, dropping to 0.7 for the L model at
300 degree 7, for example, which may relate to the influence of magnetic diffusion in their forecasting approach.
301 The per-coefficient differences in Figure 9 (left) reach up to 15 nT/yr. The azimuthal power spectrum is
302 shown in the right panel.

303 The maps of the differences in the vertical component of the candidates to the robust Huber model are
304 shown in Figure 10. For the B, CU, G, IZ, L and M candidates, most of the variation is around the western
305 and central Pacific regions, which have been experiencing a strong geomagnetic jerk over the past five years.
306 Models K, N, and S show hemispherical or degree 2 variations and deviate significantly from the robust
307 Huber model.

308 Comparison of candidate models with ground observatory data

309 Another manner in which to judge the validity and accuracy of the IGRF candidates is to compare them
310 with (semi-)independent data from the ground observatory network. Many candidates do include observatory
311 information in some form though it is usually only a small fraction of the data used.

312 In Figure 11, we examine the SV measured at twelve observatories around the world. The SV data are
313 monthly mean values derived from selected quiet-time hourly means, which were computed from the raw
314 observatory data using the procedure of [Macmillan and Olsen \(2013\)](#). We plot the monthly mean data from
315 2015.0 to 2019.5. The observed values of the vertical component are shown as grey circles. The IGRF-12
316 predicted SV between 2015 and 2020 is plotted in dotted blue. The forecasted SV from the candidates, as
317 well as the mean, median and robust models are shown as colored lines extending from 2020 to 2025. For
318 most of the observatories, the predicted SV from IGRF-12 is in reasonably good agreement at 2015.0 but
319 becomes worse for later years due to unmodeled secular acceleration. The 2014 geomagnetic jerk ([Torta et al,](#)
320 [2015](#)) caused strong acceleration for several years in certain locations, which is particularly evident in the

321 IRT, HON, KAK, and GUA datasets. The SV at HER appears to have been poorly predicted at 2015.0 (at
 322 40 nT/yr) compared to its true value (around 60 nT/yr).

323 The candidate forecasts have a wide scatter; for example at HON, the G candidate predicts SV of -12 nT/yr
 324 while the S candidate suggests almost $+30$ nT/yr. The median, mean and Huber are close, with a central
 325 forecast around -5 nT/yr. The forecasts are closer at CKI or BOU, though often there are outlier candidates
 326 e.g. the N model at SFS or KAK. In general, Figure 11 illustrates the difficulty associated with making a
 327 simple linear forecast of a complex and dynamic system.

328 Retrospective analysis of IGRF-12 secular variation models

Some insight may be gained into secular variation forecasting by investigating the performance of the IGRF-12 candidate models over their forecast period of 2015.0 to 2020.0. We compared the secular variation predictions of the IGRF-12 candidate models with both SV derived from ground observatory measurements and SV provided by the final IGRF-13 model over the 2015.0 to 2020.0 time period. For the observatory analysis, we started from the hourly mean database compiled by the British Geological Survey (Macmillan and Olsen, 2013) with data until August 2019. Data were selected for geomagnetically quiet conditions (ap index ≤ 10), and dayside ionospheric contributions were minimized by selecting data between midnight and 05:00 local time. Only observatories equatorward of $\pm 55^\circ$ QD latitude were used to minimize contamination from polar ionospheric current systems, resulting in a total of $M = 42$ stations. We fit cubic splines with knot separations of 1 year to the individual B_x , B_y , and B_z components of each station for the time interval January 2006 through August 2019. These splines were then linearly extrapolated to 2020.0 by using the spline's slope at the last knot. Figure 12 presents the analysis for the Honolulu (HON) observatory. The right panels show the original B_x (top), B_y (middle), B_z (bottom) measurements in blue, the remaining data after quiet-time selection in green, and the spline fit in black. The left panels show, for the same B_x, B_y, B_z components, annual differences of the selected observatory data in black, annual differences of the fitted spline in red, and the predictions of each IGRF-12 candidate model, including the mean, median, and final IGRF-12 SV model over the 2015.0-2020.0 time period. Note that the LN model refers to LPG Nantes, which was not a lead institute for IGRF-13. We can see that HON experienced a significant geomagnetic jerk around 2014 with a strong acceleration after the 2015.0 epoch in the B_z component, which all forecast models failed to capture. This jerk has been analyzed by Torta *et al* (2015) and Kotzé (2017). We define $S_{c,j}(t)$ as the c -th component ($c = x, y, z$) spline fitted to the magnetic field data at the observatory j , with $1 \leq j \leq M$, in units of nT, with the annual difference spline

$$\dot{S}_{c,j}(t) = S_{c,j}(t + 6 \text{ months}) - S_{c,j}(t - 6 \text{ months}) \quad (10)$$

in units of nT/year. Then the rms difference between IGRF-12 candidate model i and the observatory-derived splines, integrated over the 5-year time interval is given by

$$RMS_{c,i} = \sqrt{\frac{1}{M} \sum_{j=1}^M \frac{1}{\Delta t} \int_{2015}^{2020} \left(\dot{S}_{c,j}(t) - \dot{B}_{c,i}(\mathbf{r}_j) \right)^2 dt} \quad (11)$$

where $\Delta t = 5$ years and $\dot{B}_{c,i}(\mathbf{r}_j)$ is the secular variation of the field component c due to IGRF-12 candidate i at the observatory site \mathbf{r}_j . The rms values are presented in Table 6. With one exception, all lead institutes which provided a secular variation model for IGRF-12 also submitted a model for IGRF-13, and so we use the same institution letter codes as given in Table 1. The B-12 model exhibits the closest agreement to the observatory splines in the B_y component, while the IP-12 model shows the lowest rms difference in the B_x and B_z components. The B-12 secular variation estimate was built from modeling core flow velocity and acceleration initialized using Swarm data prior to the model epoch of 2015.0 and then stepped forward in time to 2020.0 using physically realistic constraints (Hamilton *et al.*, 2015). The IP-12 secular variation model was built using an empirical Swarm-based model at epoch 2014.3, which served as the initial condition for a 3D geodynamo model which was integrated forward in time to 2020.0 (Fournier *et al.*, 2015). The superior performance of these two models suggests that secular variation forecasting could benefit by incorporating physics-based modeling of core dynamics. The median of all IGRF-12 candidates outperformed the mean model as well as the final robust Huber-weighted IGRF-12 model in the B_x and B_z components with a slightly worse performance in the B_y component.

It is also instructive to compare the IGRF-12 candidates with the final IGRF-13 SV model over 2015.0-2020.0. We note that because the IGRF-13 main field model for 2020.0 is provisional, the SV model over 2015.0 to 2020.0 will change in a future IGRF generation. However for the purposes of analyzing the IGRF-12 candidates we will consider this model to represent the truth during this time interval. Figure 13 presents spatial map differences of dB_z/dt between the IGRF-12 SV candidates and the IGRF-13 SV model over 2015.0 to 2020.0. While there exist small-scale differences between the different maps, all IGRF-12 candidates exhibit similar large-scale differences against IGRF-13. We attribute these structures to the global secular acceleration patterns associated with the 2014 geomagnetic jerk (see Torta *et al.* (2015, Fig. 3)). The global structure of the field accelerations due to this geomagnetic jerk were unavailable in the datasets used to construct the IGRF-12 candidates, and so none of them were able to accurately account for these signals over their forecast period of 2015.0 to 2020.0.

354 **Final IGRF-13 models**

355 [Thébault et al \(2015\)](#) provided an extensive discussion on the various methodologies available for weighting
356 the candidate models submitted to the IGRF-12 call. For the IGRF-13 call, we have found the candidates
357 are, in general, much closer to each other than in previous generations. The mean, median and robust Huber
358 models derived from the DGRF-2015 and IGRF-2020 candidates exhibit close agreement with each other.
359 For the SV-2020-2025 candidates there was a wider divergence in the candidates with strong differences
360 between the more extreme ranges of the forecasts.

361 The IGRF-13 evaluation panel voted on the proposed methods for combining the candidate models. The
362 choices for the DGRF-2015 and IGRF-2020 models were to use a median of the Gauss coefficients or the
363 spatial Huber-weighting method. For the SV-2020-2025 model, the median of the Gauss coefficients and
364 spatial Huber-weighting were again proposed, as well as an additional suggestion of the simple average of
365 models B, IP, IS, L, M, and P only, in order to exclude the most different candidates. The panel voted in
366 favor (though not unanimously) to use the median of the candidates for the DGRF-2015 and IGRF-2020
367 to compute the final coefficients. For the SV-2020-2025, the panel voted to use the robust Huber-weighted
368 model in space to compute the Gauss coefficients.

369 Finally, we clarify the process for computing the final coefficient values. For the DGRF-2015 and IGRF-
370 2020 coefficients, all candidate models were rounded to two decimal places, if not already provided in this
371 format. For DGRF-2015, the median of the Gauss coefficients for each SH degree and order was computed
372 to two decimal places. For the IGRF-2020 there were an even number of candidate models, so the Gauss
373 coefficient median is the average of the two central coefficient values when sorted, which can occasionally
374 produce an answer with three decimal places. Those coefficients with three decimal places of resolution were
375 subsequently rounded to two decimal places before being output. The SV-2020-2025 model output of the
376 Huber robust weighting computation was rounded to two decimal places before output.

377 **Conclusion**

378 The 37 submitted candidates for the 13th generation of the International Geomagnetic Reference Field
379 (IGRF) were thoroughly analysed in order to deduce a suitable methodology for combining them into a
380 final set of models for release. A total of 15 international teams submitted candidates for consideration.
381 These teams submitted eleven candidate main field models for the definitive (DGRF) epoch 2015.0, twelve
382 candidate main field models for the IGRF epoch 2020.0, and fourteen secular variation models for the forecast
383 period covering 2020.0 to 2025.0.

384 A volunteer taskforce consisting of the authors of this paper carried out their analyses separately, reporting
385 back to the IAGA DIV V-MOD chair and co-chair. The analyses used both spectral and spatial comparisons,

386 and comparisons to independent data sets. All reports are available at the IAGA website <https://www.ngdc.noaa.gov/IAGA/vmod/IGRF13/evaluations>.
 387 Their conclusions were used to guide the final vote on
 388 the methodology for computing the final Gauss coefficients for each product.

389 The IAGA IGRF taskforce voted to use the median of the DGRF-2015 candidate Gauss coefficients as
 390 the final model, the median of the IGRF-2020 candidate Gauss coefficients as the final model and a robust
 391 Huber-weighting scheme in space for the SV-2020-2025 model. The final model coefficients were released for
 392 1st January 2020 and are freely and publicly available (Alken et al, 2020b).

393 **Competing interests**

394 The authors declare that they have no competing interests.

395 **Author's contributions**

396 P. Alken is chair of the IAGA DIV V-MOD (2019-2023) and initiated, coordinated and organised the call and delivery of the 13th generation of the
 397 IGRF. E. Thébaud is former chair (2015-2019). C. Beggan is present co-chair (2019-2023). PA, ET and CDB wrote the manuscript based on the
 398 analyses of the contributing co-authors. All other authors contributed detailed technical analyses forming the results presented. All co-authors have
 399 read and approved the manuscript.

400 **Acknowledgments**

401 The European Spatial Agency (ESA) is gratefully acknowledged for providing access to the Swarm magnetic field data. The results presented in this
 402 paper rely on data collected at magnetic observatories. We thank the national institutes that support them and INTERMAGNET for promoting high
 403 standards of magnetic observatory practice (www.intermagnet.org). [We thank Prof Richard Holme and an anonymous reviewer for their comments on the original manuscript.](#)

405 **Declarations**

406 [Availability of data and materials: Not applicable](#)

407 [Funding:](#) This work was partly funded by CNES in the framework of the project "Exploitation de la mission spatiale Swarm".

408 **Author details**

409 ¹Cooperative Institute for Research in Environmental Sciences, University of Colorado Boulder, 325 Broadway, E/NE42, Boulder, CO 80305, USA.

410 ²NOAA National Centers for Environmental Information, Boulder, CO, USA. ³Laboratoire de Planétologie et Géodynamique, UMR 6112, Université de
 411 Nantes, Université d'Angers, CNRS, Nantes, France. ⁴British Geological Survey, The Lyell Centre, Research Avenue South, Edinburgh, EH14 4AP, UK.

412 ⁵Division of Geomagnetism, DTU Space, Technical University of Denmark, Centrifugevej 356, Kongens Lyngby, 2800, Denmark. ⁶Université de Paris,
 413 Institut de physique du globe de Paris, CNRS, 75005 Paris, France. ⁷Univ. Grenoble Alpes, Univ. Savoie Mont Blanc, CNRS, IRD, IFSTTAR, ISTERRE,

414 38000 Grenoble, France. ⁸School of Earth and Environment, University of Leeds, Leeds, LS2 9JT, UK. ⁹University of Newcastle, Newcastle upon

415 Tyne, NE1 7RU, UK. ¹⁰GFZ German Research Centre for Geosciences, Telegrafenberg, 14473 Potsdam, Germany. ¹¹Division of Earth and Planetary

416 Sciences, Graduate School of Science, Kyoto University, Kitashirakawa Oiwake-cho, Sakyo-ku, Kyoto, 606-8502, Japan. ¹²Institut de physique du globe

417 de Strasbourg, Université de Strasbourg/EOST, CNRS, UMR 7516, Strasbourg, France. ¹³University of Potsdam, Am Neuen Palais 10, Potsdam,

418 Germany.

419 **References**

420 Alken P, Chulliat A, Nair M (2020a) University of Colorado / National Centers for Environmental Information IGRF-13 candidate models. Earth,
 421 Planets and Space this volume:XXX,

422 Alken P, Thébaud E, Beggan CD, Amit H, Aubert J, Baerenzung J, Bondar TN, Brown W, Califf S, Chambodut A, Chulliat A, Cox G, Finlay CC,
 423 Fournier A, Gillet N, Grayver A, Hammer MD, Holschneider M, Huder L, Hulot G, Jager T, Kloss C, Korte M, Kuang W, Kuvshinov A, Langlais B,

424 Léger JM, Lesur V, Livermore PW, Lowes FJ, Macmillan S, Mound JE, Nair M, Nakano S, Olsen N, Pavón-Carrasco FJ, Petrov VG, Ropp G,

425 Rother M, Sabaka TJ, Sanchez S, Saturnino D, Schnepf NR, Shen X, Stolle C, Tangborn A, Tøffner-Clausen L, Toh H, Torta JM, Varner J,

426 Vervelidou F, Vigneron P, Wardinski I, Wicht J, Woods A, Yang Y, Zeren Z, Zhou B (2020b) International Geomagnetic Reference Field: the

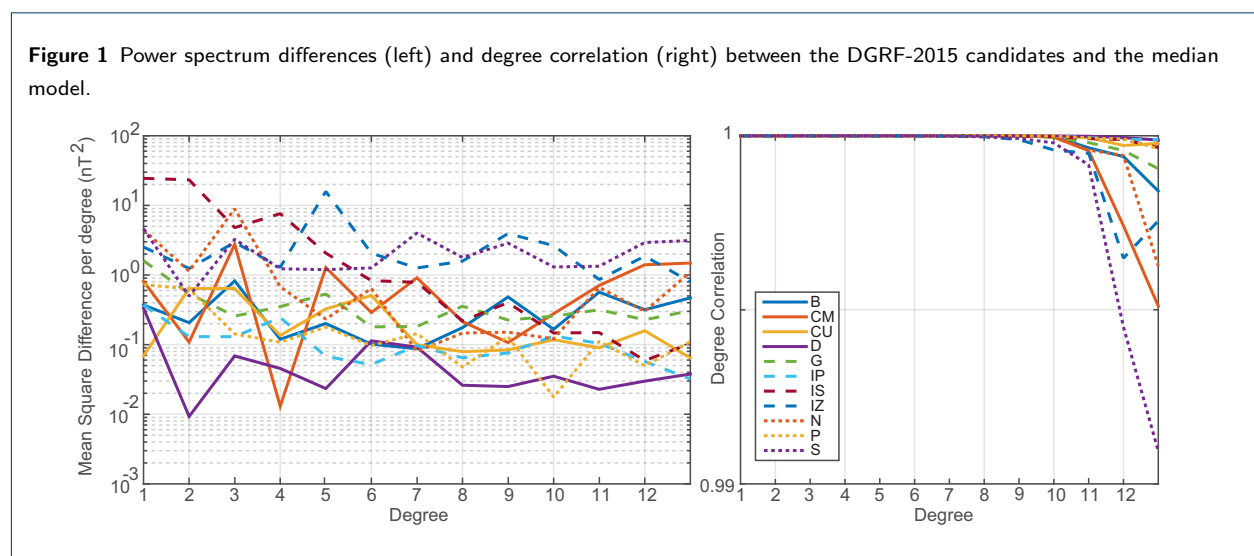
427 thirteenth generation. Earth, Planets and Space Accepted

428 Baerenzung J, Holschneider M, Lesur V, Sanchez S, Wicht J (2020) The Kalmag model as a candidate for IGRF-13. Earth, Planets and Space this

429 volume:XXX,

- 430 Bärenzung J, Holschneider M, Wicht J, Sanchez S, Lesur V (2018) Modeling and predicting the short-term evolution of the geomagnetic field. *Journal*
431 *of Geophysical Research: Solid Earth* 123(6):4539–4560,
- 432 Barton CE (1997) International geomagnetic reference field: The seventh generation. *Journal of geomagnetism and geoelectricity* 49(2-3):123–148,
- 433 Brown W, Beggan CD, Cox G, Macmillan S (2020) The BGS candidate models for IGRF-13 with a retrospective analysis of IGRF-12 secular variation
434 forecasts. *Earth, Planets and Space* this volume:XXX,
- 435 Chulliat A, Hulot G, Newitt LR (2010) Magnetic flux expulsion from the core as a possible cause of the unusually large acceleration of the north
436 magnetic pole during the 1990s. *Journal of Geophysical Research: Solid Earth* 115(B7),
- 437 Finlay CC, Maus S, Beggan CD, Hamoudi M, Lowes FJ, Olsen N, Thébault E (2010) Evaluation of candidate geomagnetic field models for IGRF-11.
438 *Earth, planets and space* 62(10):8
- 439 Finlay CC, Olsen N, Kotsiaros S, Gillet N, Tøffner-Clausen L (2016) Recent geomagnetic secular variation from Swarm and ground observatories as
440 estimated in the CHAOS-6 geomagnetic field model. *Earth, Planets and Space* 68(1):112
- 441 Finlay CC, Kloss C, Olsen N, Hammer M, Tøffner-Clausen L, Grayver A, Kuvshinov A (2020) The CHAOS-7 geomagnetic field model and observed
442 changes in the South Atlantic Anomaly. *Earth, Planets and Space* Submitted
- 443 Fournier A, Aubert J, Thébault E (2015) A candidate secular variation model for IGRF-12 based on Swarm data and inverse geodynamo modelling.
444 *Earth, Planets and Space* 67(1):81
- 445 Fournier A, Aubert J, Lesur V, Ropp G (2020) A secular variation candidate model for IGRF-13 based on Swarm data and ensemble inverse geodynamo
446 modelling. *Earth, Planets and Space* this volume:XXX,
- 447 Fratter I, Léger JM, Bertrand F, Jager T, Hulot G, Brocco L, Vigneron P (2016) Swarm absolute scalar magnetometers first in-orbit results. *Acta*
448 *Astronautica* 121:76–87
- 449 Hamilton B, Ridley VA, Beggan CD, Macmillan S (2015) The BGS magnetic field candidate models for the 12th generation IGRF. *Earth, Planets and*
450 *Space* 67(1):69
- 451 Huber PJ (1981) *Robust Statistics*. John Wiley and Sons
- 452 Huder L, Gillet N, Finlay CC, Hammer MD, Tchoungui H (2020) COV-OBS.x2: 180 yr of geomagnetic field evolution from ground-based and satellite
453 observations. *Earth, Planets and Space* Accepted
- 454 Kotzé P (2017) The 2014 geomagnetic jerk as observed by southern African magnetic observatories. *Earth, Planets and Space* 69(1):17
- 455 Langel RA, Hinze WJ (1998) *The magnetic field of the Earth's lithosphere: The satellite perspective*. Cambridge University Press
- 456 Léger JM, Jager T, Bertrand F, Hulot G, Brocco L, Vigneron P, Lalanne X, Chulliat A, Fratter I (2015) In-flight performance of the Absolute Scalar
457 Magnetometer vector mode on board the Swarm satellites. *Earth, Planets and Space* 67(1):1–12
- 458 Leopardi P (2006) A partition of the unit sphere into regions of equal area and small diameter. *Electronic Transactions on Numerical Analysis*
459 25(12):309–327
- 460 Livermore P, Finlay C, Bayliff M (2020) Recent north magnetic pole acceleration towards Siberia caused by flux lobe elongation. *Nat Geosci*
461 13:387–391,
- 462 Lowes FJ (1966) Mean-square values on sphere of spherical harmonic vector fields. *Journal of Geophysical Research* (1896-1977) 71(8):2179–2179, ,
463 URL <https://agupubs.onlinelibrary.wiley.com/doi/abs/10.1029/JZ071i008p02179>
- 464 Lowes FJ (1974) Spatial Power Spectrum of the Main Geomagnetic Field, and Extrapolation to the Core. *Geophysical Journal International*
465 36(3):717–730, , URL <https://doi.org/10.1111/j.1365-246X.1974.tb00622.x>
- 466 Macmillan S, Finlay CC (2011) The International Geomagnetic Reference Field. In: Manda M, Korte M (eds) *Geomagnetic Observations and Models*,
467 vol 5, Springer, pp 265–276
- 468 Macmillan S, Olsen N (2013) Observatory data and the Swarm mission. *Earth, Planets and Space* 65(11):15,
- 469 Maus S, Silva L, Hulot G (2008a) Can core-surface flow models be used to improve the forecast of the Earth's main magnetic field? *Journal of*
470 *Geophysical Research: Solid Earth* 113(B8),
- 471 Maus S, Yin F, Lühr H, Manoj C, Rother M, Rauberg J, Michaelis I, Stolle C, Müller RD (2008b) Resolution of direction of oceanic magnetic
472 lineations by the sixth-generation lithospheric magnetic field model from CHAMP satellite magnetic measurements. *Geochemistry, Geophysics,*
473 *Geosystems* 9(7),
- 474 Metman MC, Beggan CD, Livermore PW, Mound JE (2020) Forecasting yearly geomagnetic variation through sequential estimation of core flow and
475 magnetic diffusion. *Earth, Planets and Space* this volume:XXX,
- 476 Minami T, Nakano S, Lesur V, Takahashi F, Matsushima M, Shimizu H, Nakashima R, Taniguchi H, Toh H (2020) A candidate secular variation model
477 for IGRF-13 based on MHD dynamo simulation and 4DnVar data assimilation. *Earth, Planets and Space*
- 478 Olsen N, Lühr H, Finlay CC, Sabaka TJ, Michaelis I, Rauberg J, Tøffner-Clausen L (2014) The CHAOS-4 geomagnetic field model. *Geophysical*
479 *Journal International* 197(2):815–827,

- 480 Pavón-Carrasco FJ, Marsal S, Torta JM, Catalán M, Martín-Hernández F, Tordesillas JM (2020) Bootstrapping Swarm and observatory data to
 481 generate candidates for the DGRF and IGRF-13. *Earth, Planets and Space*
- 482 Petrov VG, Bondar TN (2020) IZMIRAN sub-model for IGRF-13. *Earth, Planets and Space* this volume:XXX,
- 483 Ropp G, Lesur V, Baerenzung J, Holschneider M (2020) Sequential modelling of the Earth's core magnetic field. *Earth, Planets and Space* Under review
- 484 Rother M, Korte M, Morschhauser A, Vervelidou F, Matzka J, Stolle C (2020) The Mag.num core field model as a parent for IGRF-13, and the recent
 485 evolution of the South Atlantic Anomaly. *Earth, Planets and Space* Submitted
- 486 Sabaka TJ, Tøffner-Clausen L, Olsen N, Finlay CC (2020) CM6: A Comprehensive Geomagnetic Field Model Derived From Both CHAMP and Swarm
 487 Satellite Observations. *Earth, Planets and Space* Submitted
- 488 Sanchez S, Wicht J, Bärenzung J (2020) Predictions of the geomagnetic secular variation based on the ensemble sequential assimilation of
 489 geomagnetic field models by dynamo simulations. *Earth, Planets and Space* Submitted
- 490 Shen X, Zhang X, Yuan S, Wang L, Cao J, Huang J, Zhu X, Piergiorgio P, Dai J (2018) The state-of-the-art of the China Seismo-Electromagnetic
 491 Satellite mission. *Science China Technological Sciences* 61(5):634–642,
- 492 Tangborn A, Kuang W, Sabaka TJ, Yi C (2020) Geomagnetic secular variation forecast using the NASA GEMS ensemble Kalman filter: A candidate
 493 model for IGRF 2020. *Earth, Planets and Space*
- 494 Thébaud E, Finlay CC, Alken P, Beggan CD, Canet E, Chulliat A, Langlais B, Lesur V, Lowes FJ, Manoj C, Rother M, Schachtschneider R (2015)
 495 Evaluation of candidate geomagnetic field models for IGRF-12. *Earth, Planets, and Space* 67:112,
- 496 Torta JM, Pavón-Carrasco FJ, Marsal S, Finlay CC (2015) Evidence for a new geomagnetic jerk in 2014. *Geophysical Research Letters*
 497 42(19):7933–7940,
- 498 Vigneron P, Hulot G, Léger JM, Jager T (2020) A 2015 Definitive Geomagnetic Reference Field (DGRF) Candidate Model Based on Swarm's
 499 Experimental Absolute Magnetometer Vector Mode Data. *Earth, Planets and Space* In preparation
- 500 Wardinski I, Saturnino D, Amit H, Chambodut A, Langlais B, Mandea M, Thébaud E (2020) Geomagnetic core field models and secular variation
 501 forecasts for the 13th International Geomagnetic Reference Field (IGRF-13). *Earth, Planets and Space* In preparation
- 502 Whaler KA, Beggan CD (2015) Derivation and use of core surface flows for forecasting secular variation. *Journal of Geophysical Research: Solid Earth*
 503 120(3):1400–1414,
- 504 Winch DE, Ivers DJ, Turner JPR, Stening RJ (2005) Geomagnetism and Schmidt quasi-normalization. *Geophysical Journal International*
 505 160(2):487–504, URL <https://doi.org/10.1111/j.1365-246X.2004.02472.x>,
 506 <https://academic.oup.com/gji/article-pdf/160/2/487/5970028/160-2-487.pdf>
- 507 Yang Y, Hulot G, Vigneron P, Shen X, Zeren Z, Zhou B, Magnes W, Olsen N, Tøffner-Clausen L, Huang J, Zhang X, Wang L, Cheng B, Pollinger A,
 508 Lammegger R, Lin J, Guo F, Yu J, Wang J, Wu Y, Zhao X (2020) The CSES Global Geomagnetic Field Model (CGGM): An IGRF type global
 509 geomagnetic field model based on data from the China Seismo-Electromagnetic Satellite. *Earth, Planets and Space* Submitted

510 **Figures**511 **Tables**

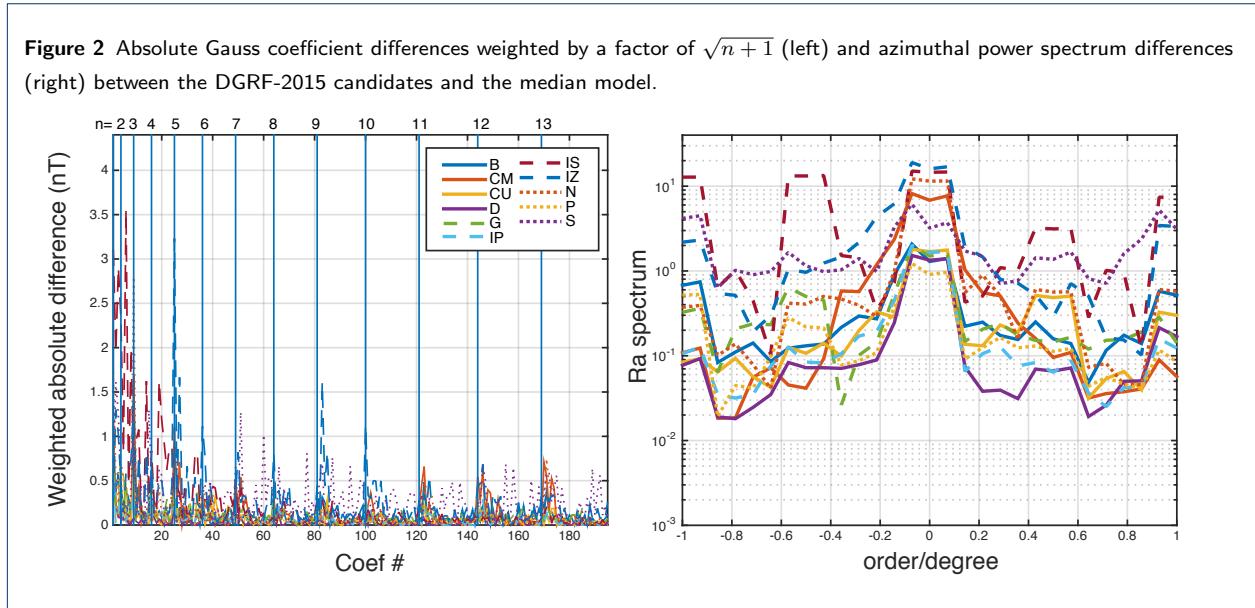


Table 1 Teams who submitted IGRF-13 candidate models

Letter Code	Lead Institute	DGRF2015	IGRF2020	SV2020-2025	Reference
B	British Geological Survey	✓	✓	✓	Brown et al (2020)
CE	China Earthquake Administration		✓		Yang et al (2020)
CM	Universidad Complutense de Madrid	✓	✓	✓	Pavón-Carrasco et al (2020)
CU	University of Colorado Boulder	✓	✓	✓	Alken et al (2020a)
D	Technical University of Denmark (DTU Space)	✓	✓	✓	Finlay et al (2020)
G	GFZ German Research Centre for Geosciences	✓	✓	✓	Rother et al (2020)
IP	Institut de physique du globe de Paris	✓	✓	✓	Fournier et al (2020); Ropp et al (2020); Vigneron et al (2020)
IS	Institut des Sciences de la Terre	✓	✓	✓	Huder et al (2020)
IZ	Pushkov Institute of Terrestrial Magnetism (IZMIRAN)	✓	✓	✓	Petrov and Bondar (2020)
K	Kyoto University			✓	Minami et al (2020)
L	University of Leeds			✓	Metman et al (2020)
M	Max Planck Institute for Solar System Research			✓	Sanchez et al (2020)
N	NASA Goddard Space Flight Center	✓	✓	✓	Sabaka et al (2020); Tangborn et al (2020)
P	University of Potsdam	✓	✓	✓	Baerenzung et al (2020)
S	Université de Strasbourg	✓	✓	✓	Wardinski et al (2020)

Table 2 Root-mean-square vector field differences i,jT in units of nT between DGRF-2015 candidate models and also between candidates and the arithmetic mean reference models M , median reference model M_{med} and robust Huber-weighted in the rightmost columns. The bottom row is the simple arithmetic mean of the columns.

$i,jT/nT$	B	CM	CU	D	G	IP	IS	IZ	N	P	S	M	M_{med}	robust
B	0.00	4.51	2.53	2.17	2.68	2.63	8.53	6.54	4.43	2.53	6.12	2.25	2.02	1.97
CM	4.51	0.00	3.77	3.21	4.69	3.13	8.87	7.44	6.18	3.85	6.09	3.45	3.22	3.37
CU	2.53	3.77	0.00	1.70	3.13	2.05	8.23	6.83	4.26	2.71	5.84	1.96	1.74	1.75
D	2.17	3.21	1.70	0.00	2.77	1.15	8.30	6.48	4.41	1.80	5.87	1.52	0.93	1.11
G	2.68	4.69	3.13	2.77	0.00	3.12	8.27	6.17	4.22	2.36	5.71	2.12	2.31	2.11
IP	2.63	3.13	2.05	1.15	3.12	0.00	8.19	6.50	4.88	2.08	5.82	1.76	1.25	1.47
IS	8.53	8.87	8.23	8.30	8.27	8.19	0.00	11.39	9.06	8.01	10.04	7.57	8.06	7.89
IZ	6.54	7.44	6.83	6.48	6.17	6.50	11.39	0.00	7.87	6.43	8.09	6.01	6.23	6.14
N	4.43	6.18	4.26	4.41	4.22	4.88	9.06	7.87	0.00	4.39	6.96	4.04	4.32	4.07
P	2.53	3.85	2.71	1.80	2.36	2.08	8.01	6.43	4.39	0.00	5.84	1.69	1.58	1.46
S	6.12	6.09	5.84	5.87	5.71	5.82	10.04	8.09	6.96	5.84	0.00	5.12	5.42	5.32
Mean Diff	4.27	5.18	4.11	3.79	4.31	3.96	8.89	7.37	5.66	4.00	6.64	3.41	3.37	3.33

Figure 3 Differences (in nT) on the reference sphere $r = a$ between the vertical field (B_z) of the DGRF-2015 candidates and the median model at 2015.0.

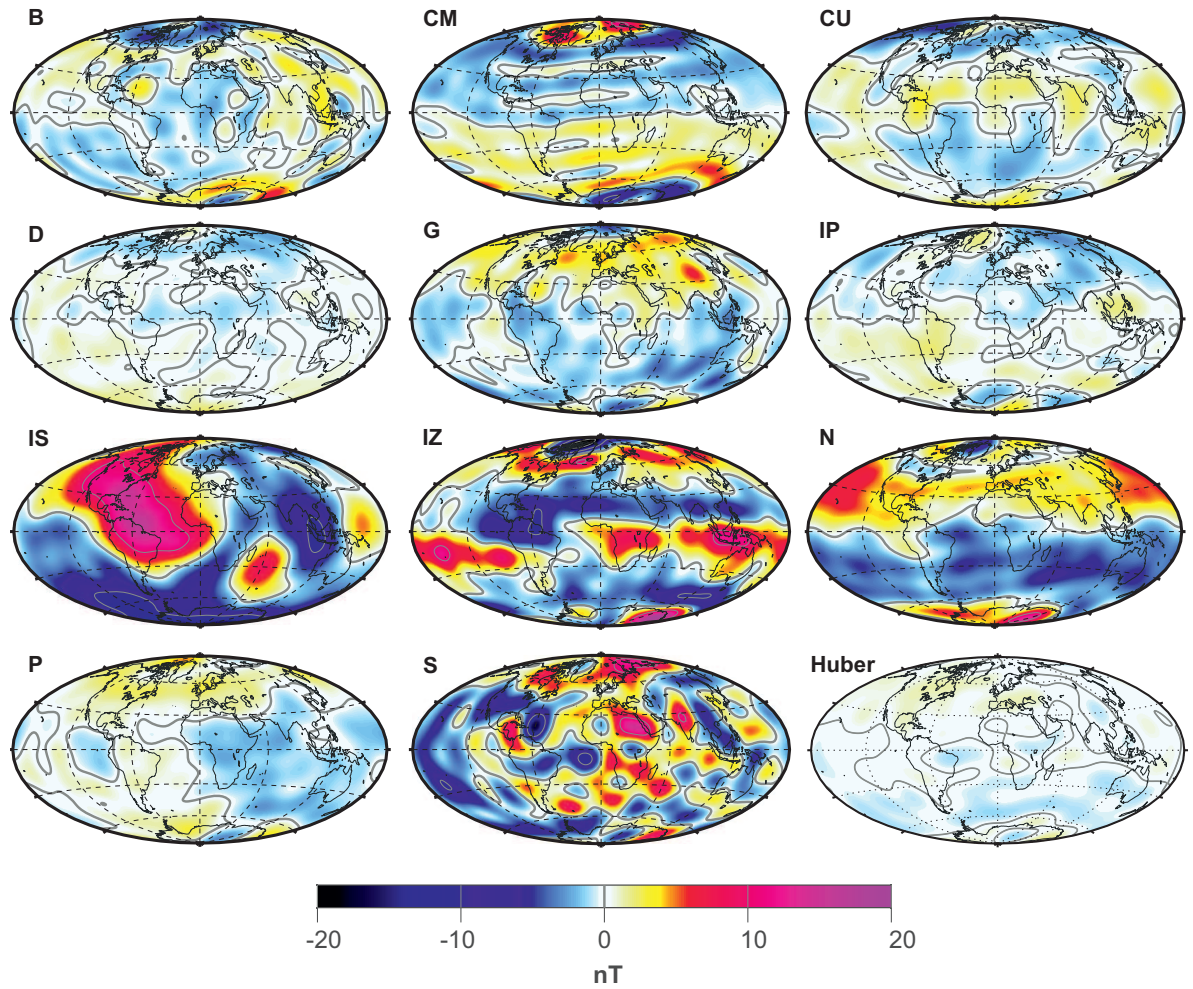


Figure 4 Vertical component (B_z) residuals between a combined Swarm A and B dataset and the DGRF-2015 candidates. The Swarm dataset spans 15 December 2014 to 15 January 2015.

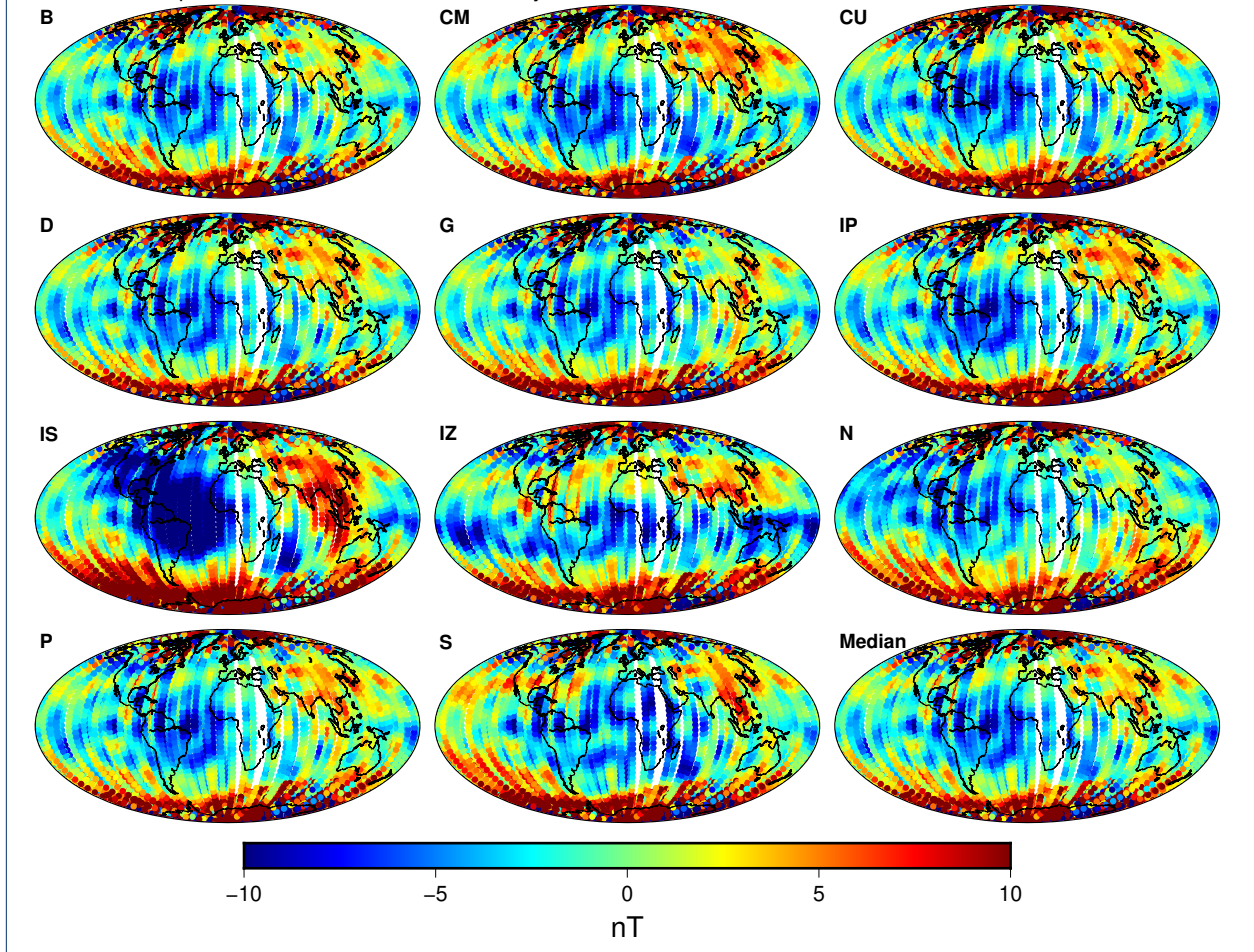


Figure 5 Power spectral differences (left) and degree correlation (right) between the IGRF-2020 candidates and the median model.

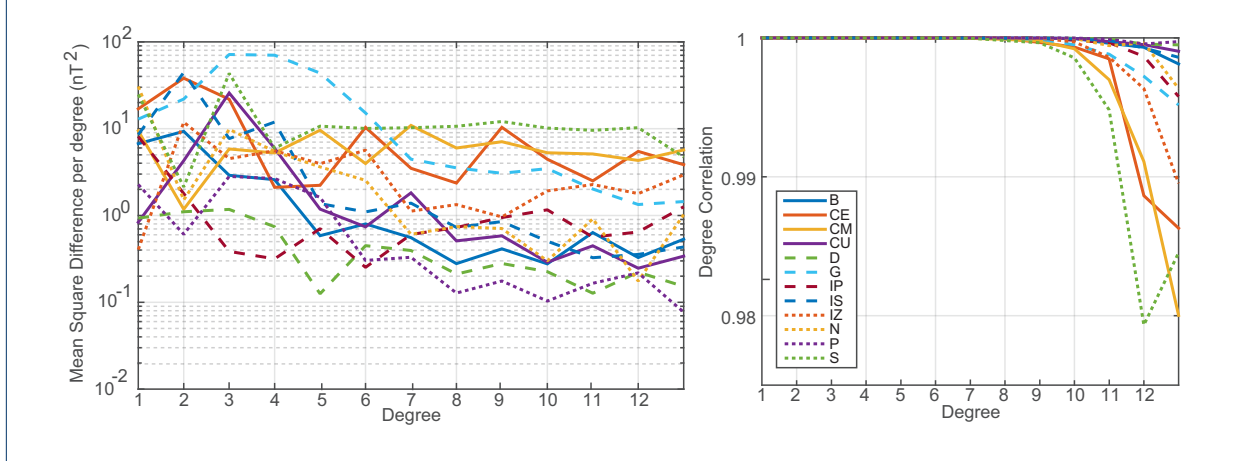


Figure 6 Absolute Gauss coefficient differences weighted by a factor of $\sqrt{n+1}$ (left) and azimuthal power spectral differences (right) between the IGRF-2020 candidates and the median model.

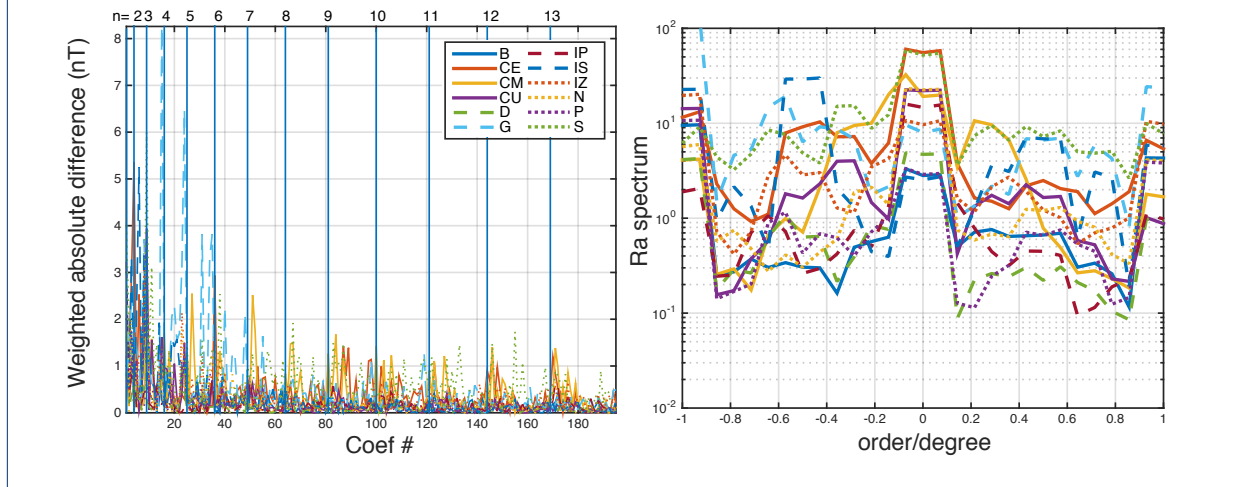


Table 3 Statistics of residuals between DGRF-2015 candidates and Swarm A/B measurements (equatorward of $\pm 55^\circ$ QD latitude) from 15 December 2014 to 15 January 2015. Vector components are given in the NEC frame.

	N	B_x		B_y		B_z		$ B $	
		mean (nT)	σ (nT)						
B	21 113	0.93	4.45	1.37	4.65	-0.41	3.87	0.11	3.81
CM	21 113	1.41	4.28	1.29	4.58	-0.38	3.96	1.53	3.75
CU	21 113	1.05	4.45	1.34	4.64	-0.49	3.96	0.36	3.66
D	21 113	1.15	4.39	1.32	4.65	-0.52	3.82	0.66	3.74
G	21 113	0.25	4.41	1.29	4.63	-0.34	3.97	-0.60	3.88
IP	21 113	1.12	4.38	1.32	4.63	-0.52	3.99	0.83	3.84
IS	21 113	-1.14	4.97	0.79	5.02	-1.00	7.32	-3.00	5.31
IZ	21 113	0.58	4.86	1.47	4.83	-0.28	4.84	0.85	4.37
N	21 113	0.19	4.87	1.38	4.75	-0.42	4.14	-1.87	3.65
P	21 113	0.65	4.40	1.26	4.62	-0.53	3.83	0.04	3.76
S	21 113	0.43	4.48	1.13	4.59	0.16	4.58	0.11	4.50
M	21 113	0.60	4.39	1.27	4.61	-0.43	4.04	-0.09	3.84
M_{med}	21 113	0.89	4.39	1.30	4.60	-0.45	3.88	0.39	3.80
robust	21 113	0.71	4.39	1.29	4.62	-0.43	3.94	0.06	3.80

Figure 7 Differences (in nT) on the reference sphere $r = a$ between the vertical field (B_z) of the IGRF-2020 candidates and the median model field values at 2020.0

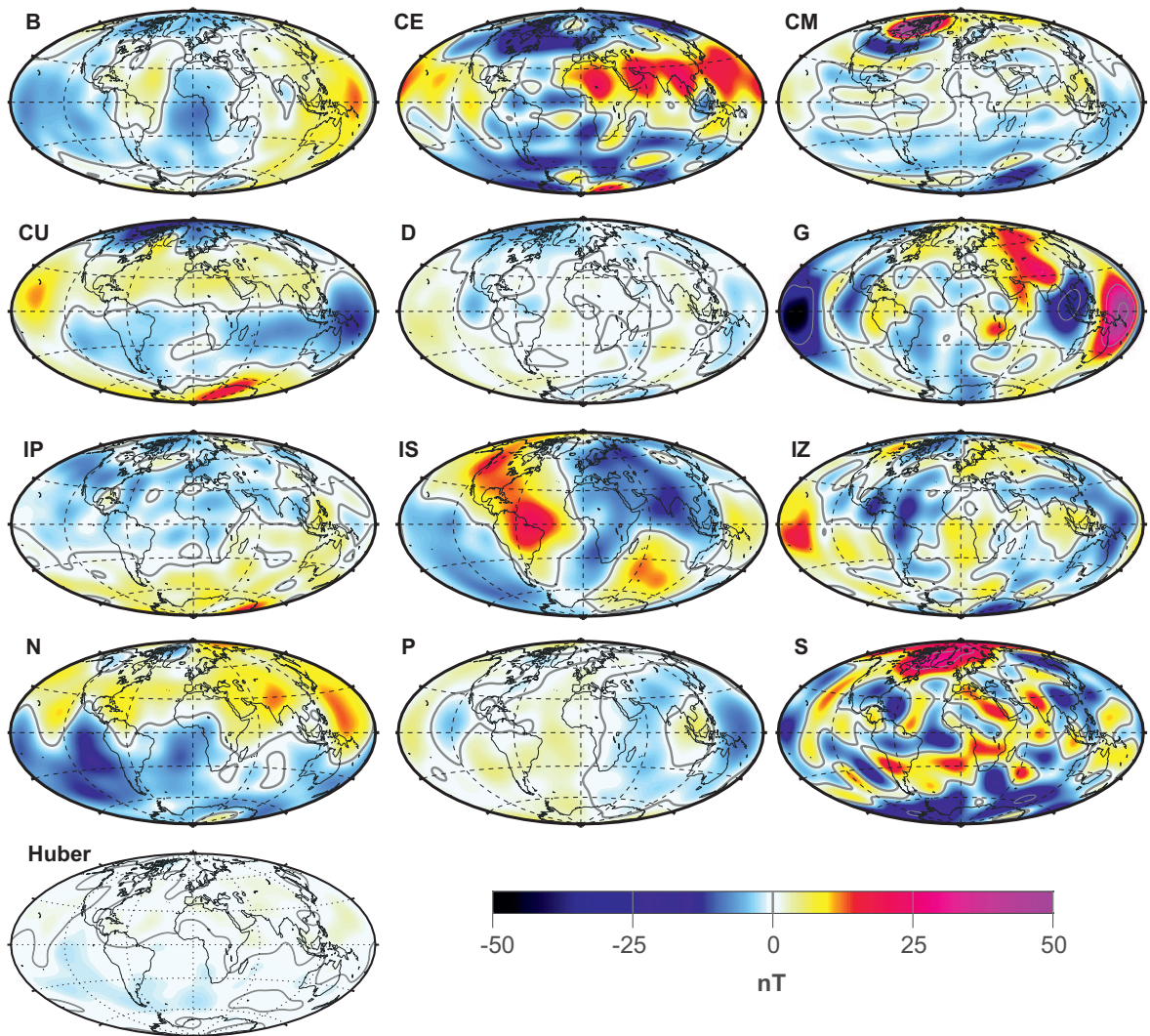


Figure 8 Power spectral differences (left) and degree correlation (right) between the SV-2020-2025 candidates and the robust model.

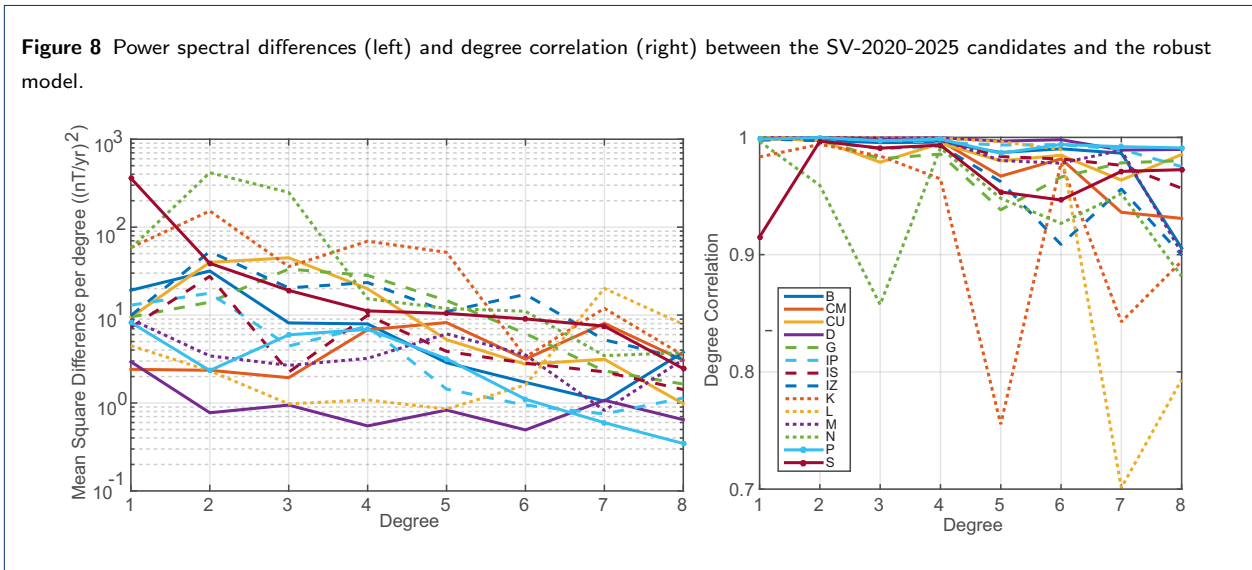


Figure 9 Absolute Gauss coefficient differences weighted by a factor of $\sqrt{n+1}$ (left) and azimuthal power spectrum difference (right) between the SV-2020-2025 candidates and the robust model.

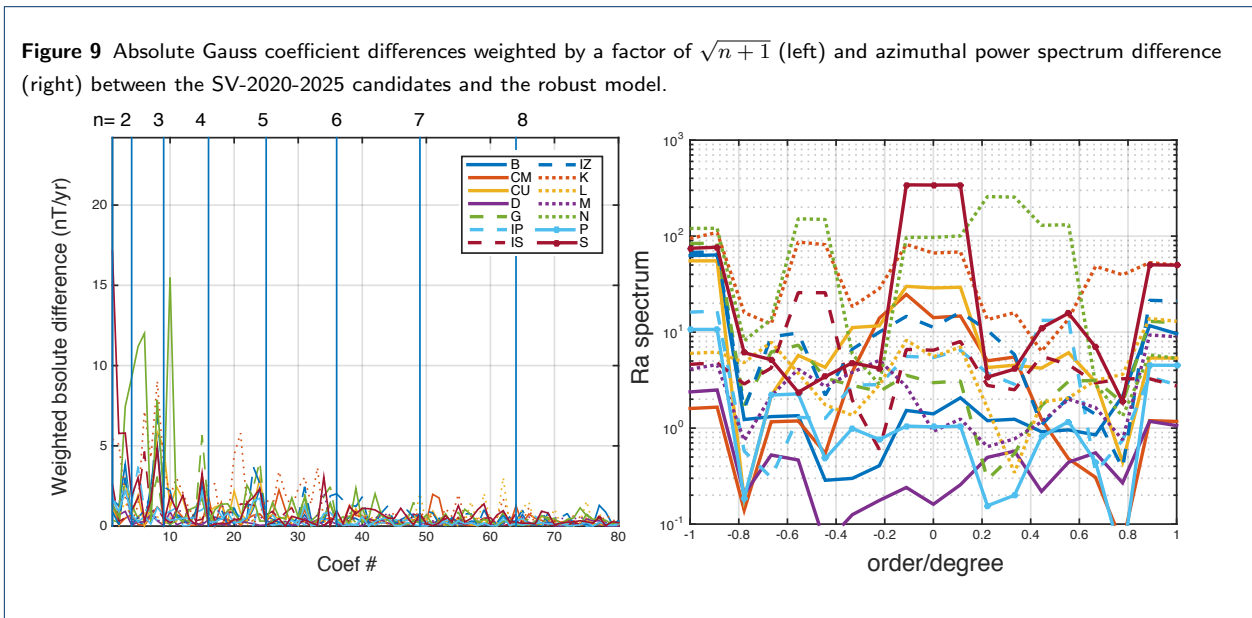


Figure 10 Annual average differences (in nT/yr) on the reference sphere $r = a$ between the vertical field (dB_z/dt) of the SV-2020-2025 candidates and the robust Huber model over 2020.0 to 2025.0.

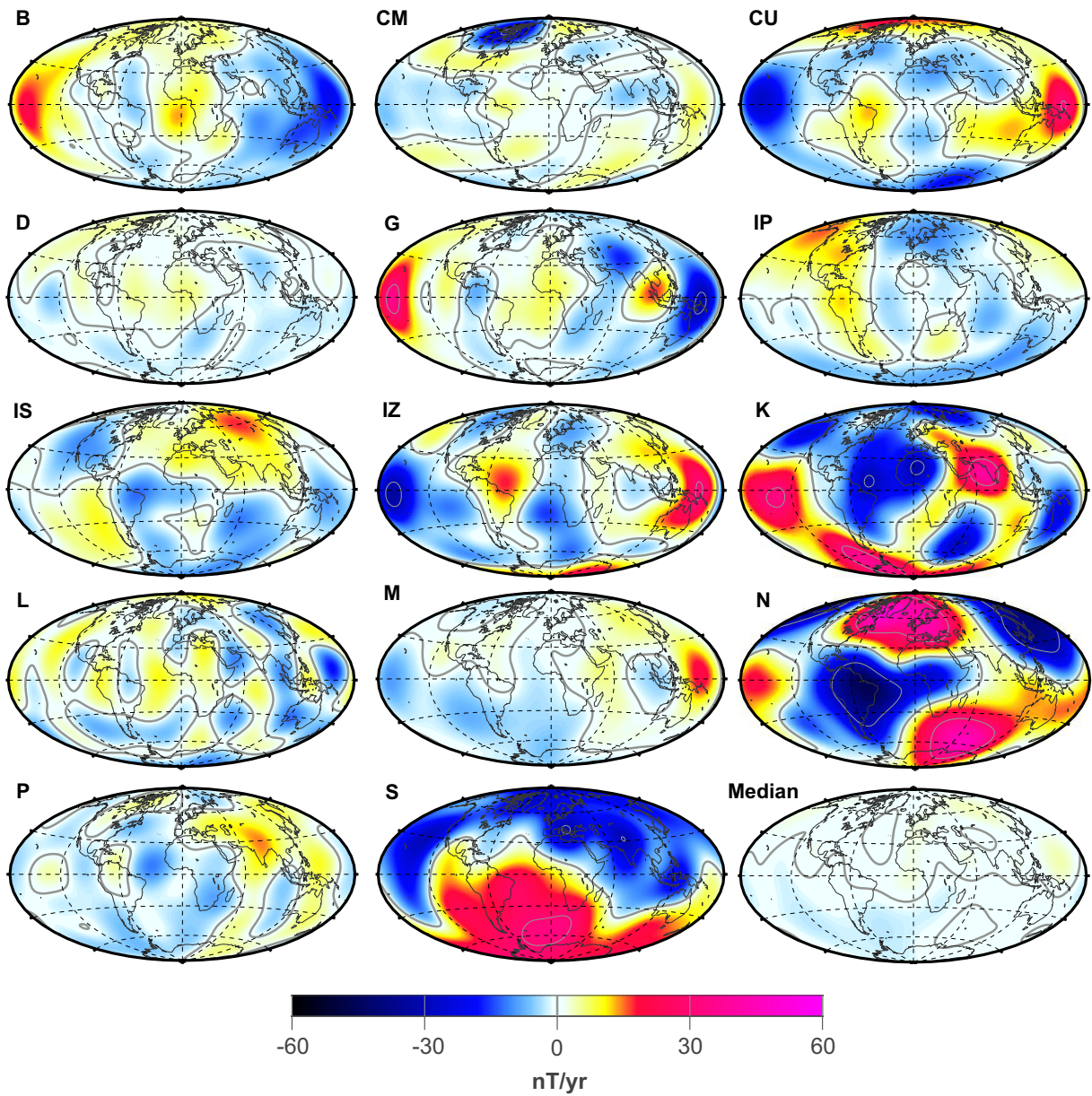


Figure 11 Comparison of the dB_z/dt component (NEC frame) of the IGRF-13 SV-2020-2025 candidates to selected observatory time-series over the 2015 to 2020 interval. The 2015–2020 SV values are from the IGRF-12 prediction.

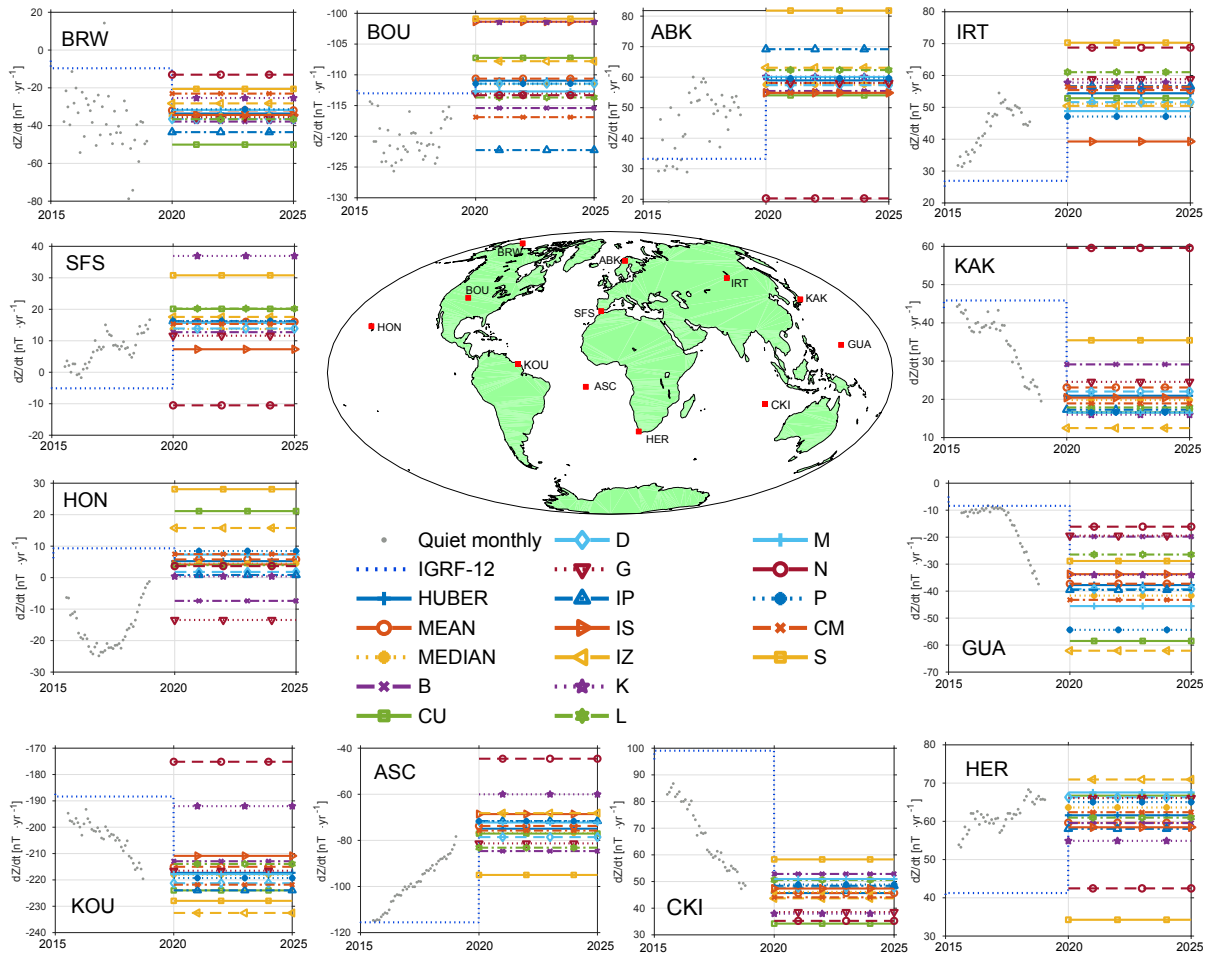


Figure 12 IGRF12 retroactive SV comparison at Honolulu (HON). Left panels show the observatory annual differences of daily mean values (black), annual spline difference curve (red) and IGRF12 candidate predictions for the dB_x/dt (top), dB_y/dt (middle), and dB_z/dt (bottom) components in the NEC frame. Right panels show the original observatory data (blue), data after selecting for geomagnetically quiet periods (green), and fitted spline curve (black) for the B_x (top), B_y (middle) and B_z (bottom) components.

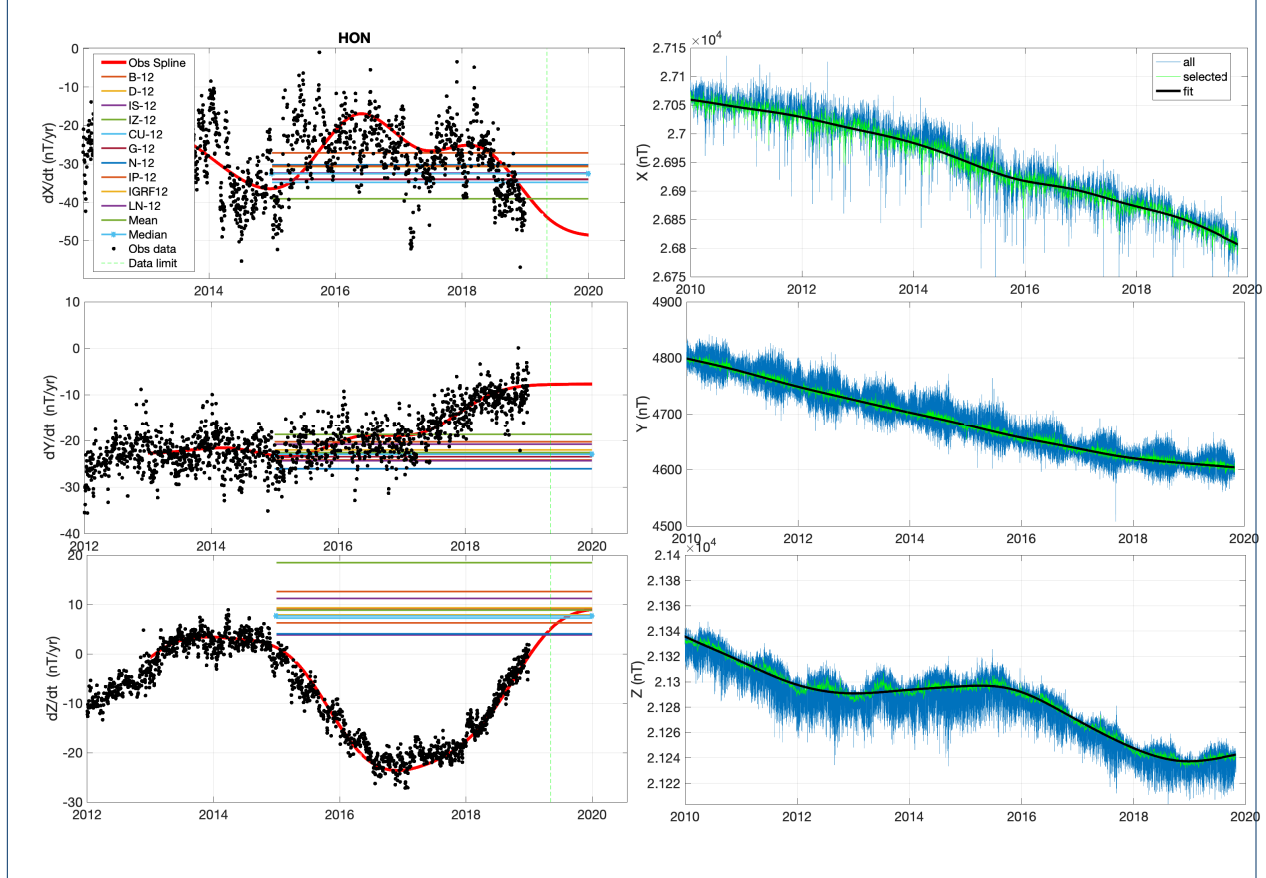


Table 4 Root-mean-square vector field differences $i_{i,j}T$ in units nT between IGRF-2020 candidate models and also between candidates and the arithmetic mean reference models M , median reference model M_{med} and robust Huber-weighted model in the rightmost columns. The bottom row is the simple arithmetic mean of the columns.

$i_{i,j}T/nT$	B	CE	CM	CU	D	G	IP	IS	IZ	N	P	S	M	M_{med}	robust
B	0.0	11.6	11.2	8.9	6.1	14.3	5.5	9.4	10.2	7.4	7.2	14.5	4.61	5.09	4.69
CE	11.6	0.0	14.7	11.9	11.2	19.5	12.7	15.7	13.9	11.0	12.5	18.1	10.56	11.14	10.60
CM	11.2	14.7	0.0	12.2	9.8	19.1	10.8	12.8	10.9	11.3	9.3	13.8	8.62	8.93	8.97
CU	8.9	11.9	12.2	0.0	6.1	19.3	7.8	12.1	8.8	9.9	6.7	16.4	7.12	6.56	6.41
D	6.1	11.2	9.8	6.1	0.0	17.1	4.8	10.0	6.4	8.5	3.6	14.0	3.69	2.48	2.95
G	14.3	19.5	19.1	19.3	17.1	0.0	16.4	17.7	20.1	15.1	18.4	19.1	14.88	15.96	15.69
IP	5.5	12.7	10.8	7.8	4.8	16.4	0.0	10.3	8.0	9.8	5.5	14.2	4.93	4.18	4.56
IS	9.4	15.7	12.8	12.1	10.0	17.7	10.3	0.0	13.2	11.4	9.7	16.2	8.93	8.93	9.03
IZ	10.2	13.9	10.9	8.8	6.4	20.1	8.0	13.2	0.0	11.7	6.2	14.8	7.69	6.66	6.98
N	7.4	11.0	11.3	9.9	8.5	15.1	9.8	11.4	11.7	0.0	9.7	14.3	6.42	7.62	6.71
P	7.2	12.5	9.3	6.7	3.6	18.4	5.5	9.7	6.2	9.7	0.0	13.8	4.74	3.39	4.00
S	14.5	18.1	13.8	16.4	14.0	19.1	14.2	16.2	14.8	14.3	13.8	0.0	12.14	12.84	12.70
Mean Diff	9.7	13.9	12.4	10.9	8.9	17.8	9.6	12.6	11.3	10.9	9.3	15.4	7.86	7.81	7.78

Figure 13 Spatial map differences of dB_z/dt (in nT/year) between IGRF-12 secular variation candidates and final IGRF-13 secular variation model over the 2015.0 to 2020.0 time period. We additionally include spatial map differences (against IGRF-13) of the mean and median of all IGRF-12 candidates, as well as the final IGRF-12 SV model in the bottom row.

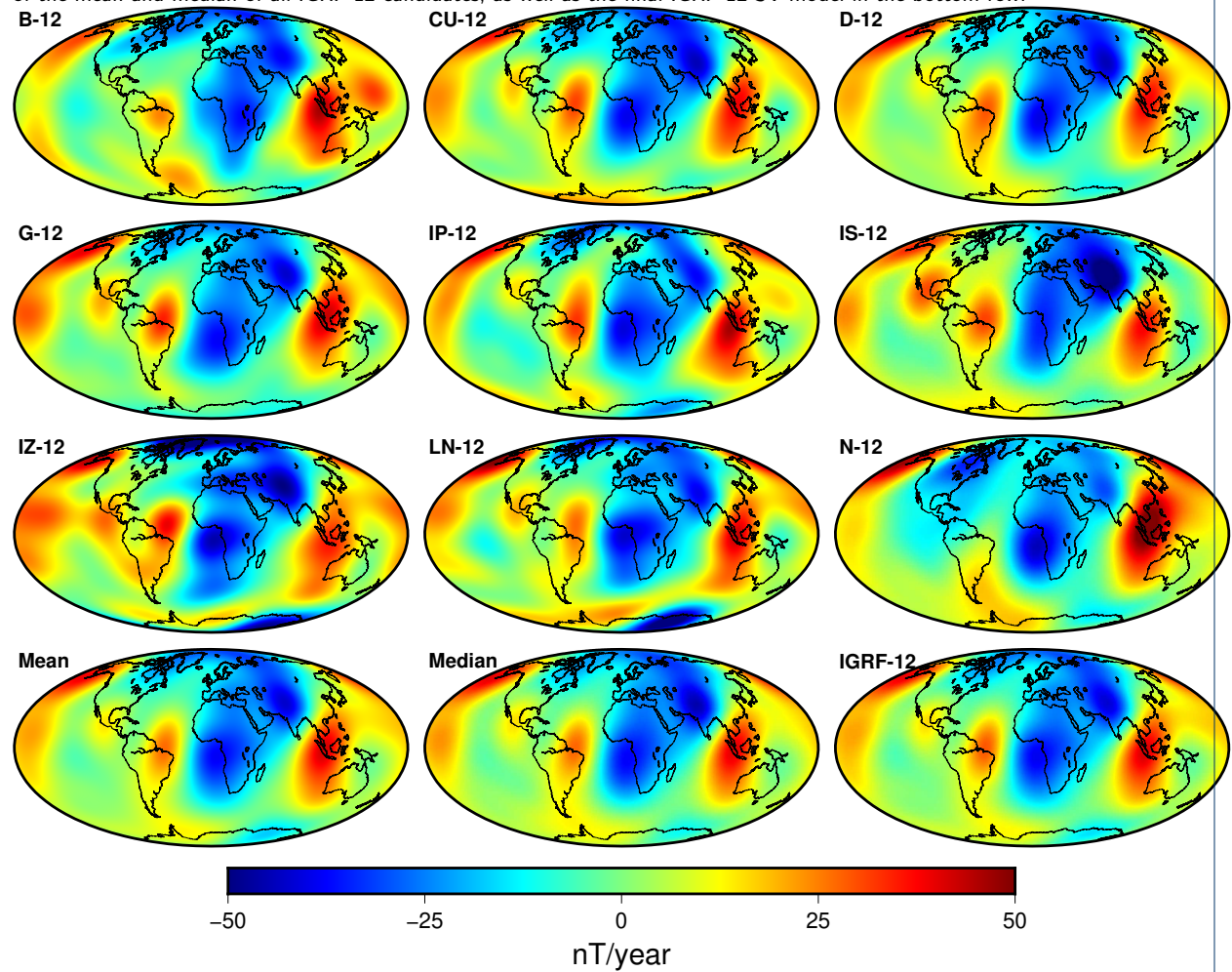


Table 5 Root-mean-square vector field differences $i_{i,j}T$ in units nT/yr between SV candidate models and also between candidates and the arithmetic mean reference models M , median reference model M_{med} and robust Huber-weighted model in the rightmost columns. The bottom row is the simple arithmetic mean of the columns.

$i_{i,j}T/nT/yr$	B	CM	CU	D	G	IP	IS	IZ	K	L	M	N	P	S	M	M_{med}	robust
B	0.0	12.0	18.1	8.3	7.6	10.4	10.7	19.5	20.7	8.5	11.6	28.2	12.6	24.4	8.89	9.04	8.74
CM	12.0	0.0	12.1	6.8	13.3	9.4	10.7	11.4	22.0	9.2	8.8	29.1	6.8	21.0	6.23	6.27	6.00
CU	18.1	12.1	0.0	11.3	19.2	12.6	14.6	10.6	26.6	13.7	12.5	32.7	9.8	23.9	11.81	10.92	11.24
D	8.3	6.8	11.3	0.0	10.1	6.8	8.3	12.2	21.3	6.7	6.8	28.8	5.9	21.9	3.88	2.42	2.87
G	7.6	13.3	19.2	10.1	0.0	12.0	12.9	20.7	21.0	11.1	13.4	29.6	14.7	24.6	10.68	10.83	10.49
IP	10.4	9.4	12.6	6.8	12.0	0.0	10.9	13.6	22.4	8.6	9.3	31.5	8.8	23.0	7.67	6.87	6.85
IS	10.7	10.7	14.6	8.3	12.9	10.9	0.0	15.6	19.3	10.2	8.6	28.8	9.7	25.0	7.78	7.51	7.58
IZ	19.5	11.4	10.6	12.2	20.7	13.6	15.6	0.0	26.3	15.1	12.0	32.6	9.3	24.4	12.39	11.61	11.96
K	20.7	22.0	26.6	21.3	21.0	22.4	19.3	26.3	0.0	21.8	19.7	32.7	21.7	29.2	18.99	20.47	19.67
L	8.5	9.2	13.7	6.7	11.1	8.6	10.2	15.1	21.8	0.0	9.1	28.9	9.1	23.3	6.81	6.68	6.27
M	11.6	8.8	12.5	6.8	13.4	9.3	8.6	12.0	19.7	9.1	0.0	28.0	6.0	24.6	6.01	5.32	5.65
N	28.2	29.1	32.7	28.8	29.6	31.5	28.8	32.6	32.7	28.9	28.0	0.0	28.5	38.0	26.67	27.92	27.72
P	12.6	6.8	9.8	5.9	14.7	8.8	9.7	9.3	21.7	9.1	6.0	28.5	0.0	23.6	5.87	4.59	5.35
S	24.4	21.0	23.9	21.9	24.6	23.0	25.0	24.4	29.2	23.3	24.6	38.0	23.6	0.0	20.96	22.40	21.43
Mean Diff	14.8	13.3	16.7	11.9	16.2	13.8	14.2	17.2	23.4	12.5	13.1	30.6	12.8	25.1	11.05	10.92	10.84

Table 6 Root-mean-square differences in nT/year between observatory-derived secular variation splines and IGRF-12 candidates over the 2015-2020 time period. The lead institute letter codes are provided in Table 1. LN refers to LPG Nantes which was not a lead institute for IGRF-13.

2015-2020	B-12	CU-12	D-12	G-12	IP-12	IS-12	IZ-12	LN-12	N-12	M	M_{med}	IGRF-12
dB_x/dt	11.76	12.10	11.64	11.53	11.20	11.68	12.41	11.65	12.81	11.47	11.31	11.47
dB_y/dt	9.35	11.22	11.24	10.92	10.64	12.99	12.04	11.05	10.37	10.71	10.87	10.75
dB_z/dt	18.42	19.2	18.54	17.78	17.33	19.73	21.60	19.41	22.16	18.39	18.03	18.50

Figures

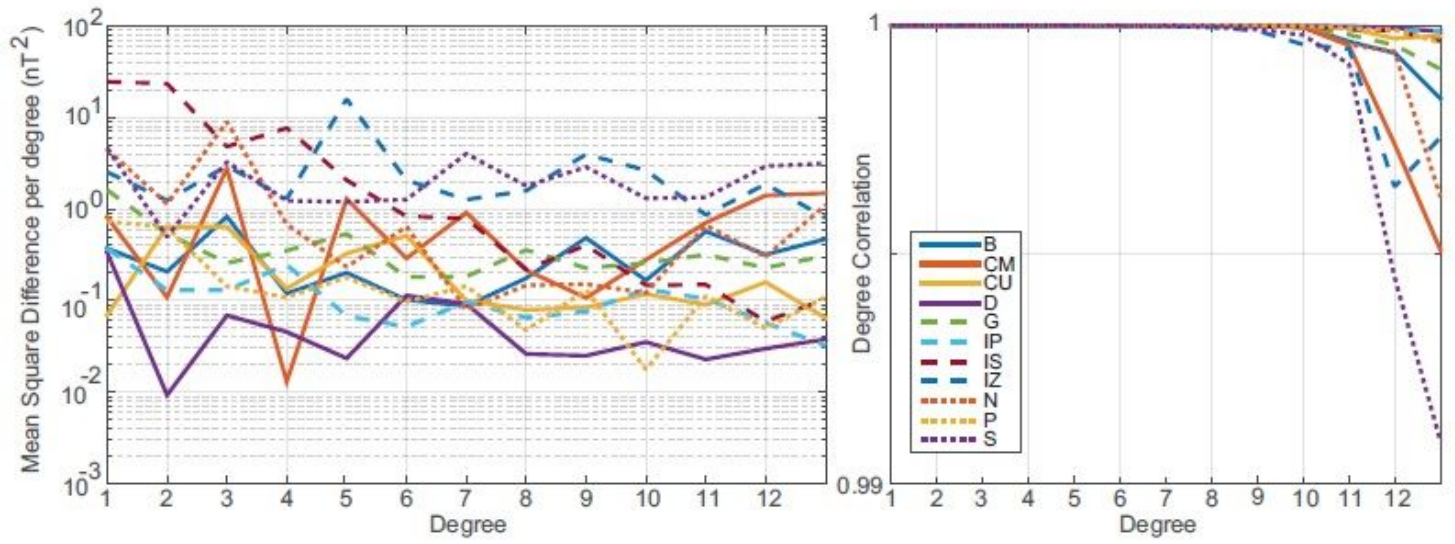


Figure 1

Power spectrum differences (left) and degree correlation (right) between the DGRF-2015 candidates and the median model.

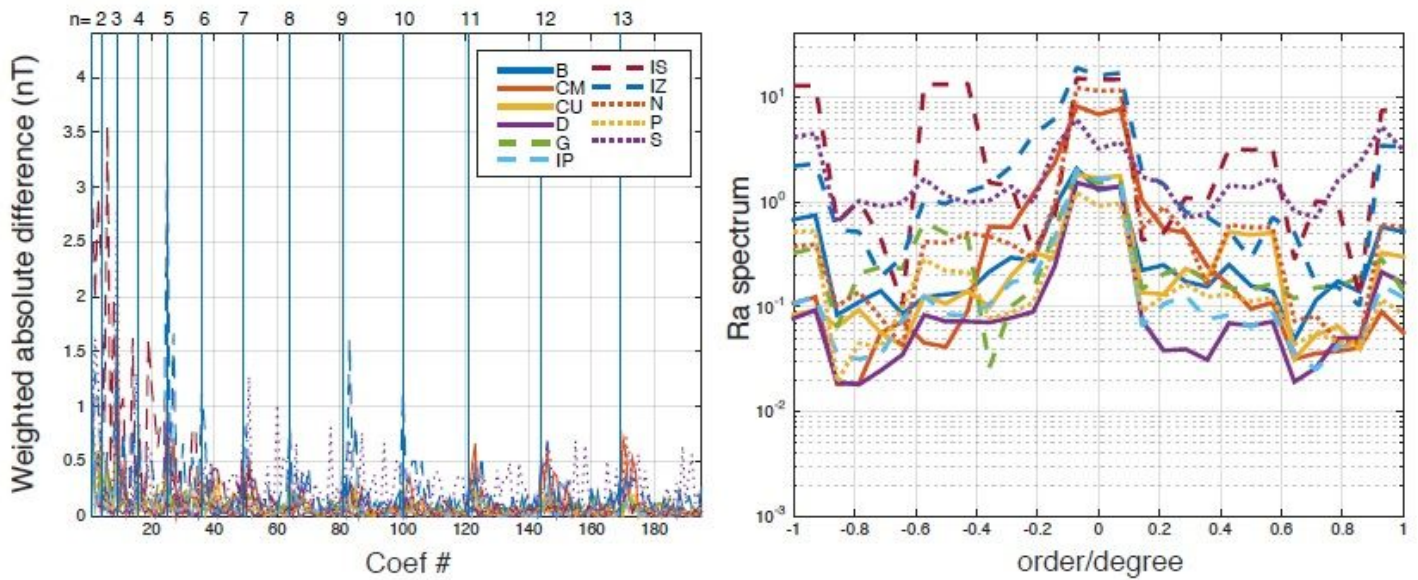


Figure 2

Absolute Gauss coefficient differences weighted by a factor of $p n + 1$ (left) and azimuthal power spectrum differences (right) between the DGRF-2015 candidates and the median model.

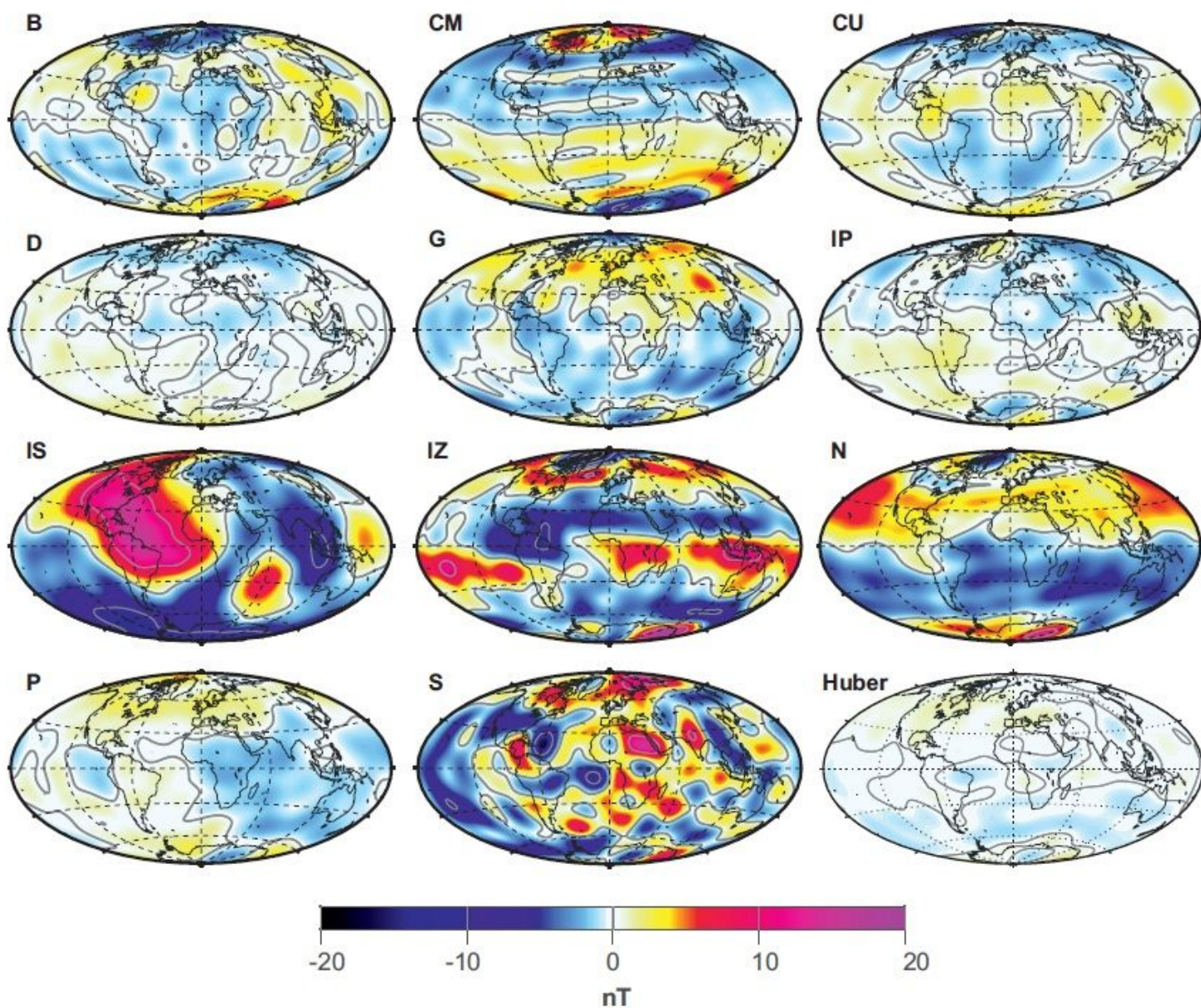


Figure 3

Differences (in nT) on the reference sphere $r = a$ between the vertical eld (B_z) of the DGRF-2015 candidates and the median model at 2015.0.

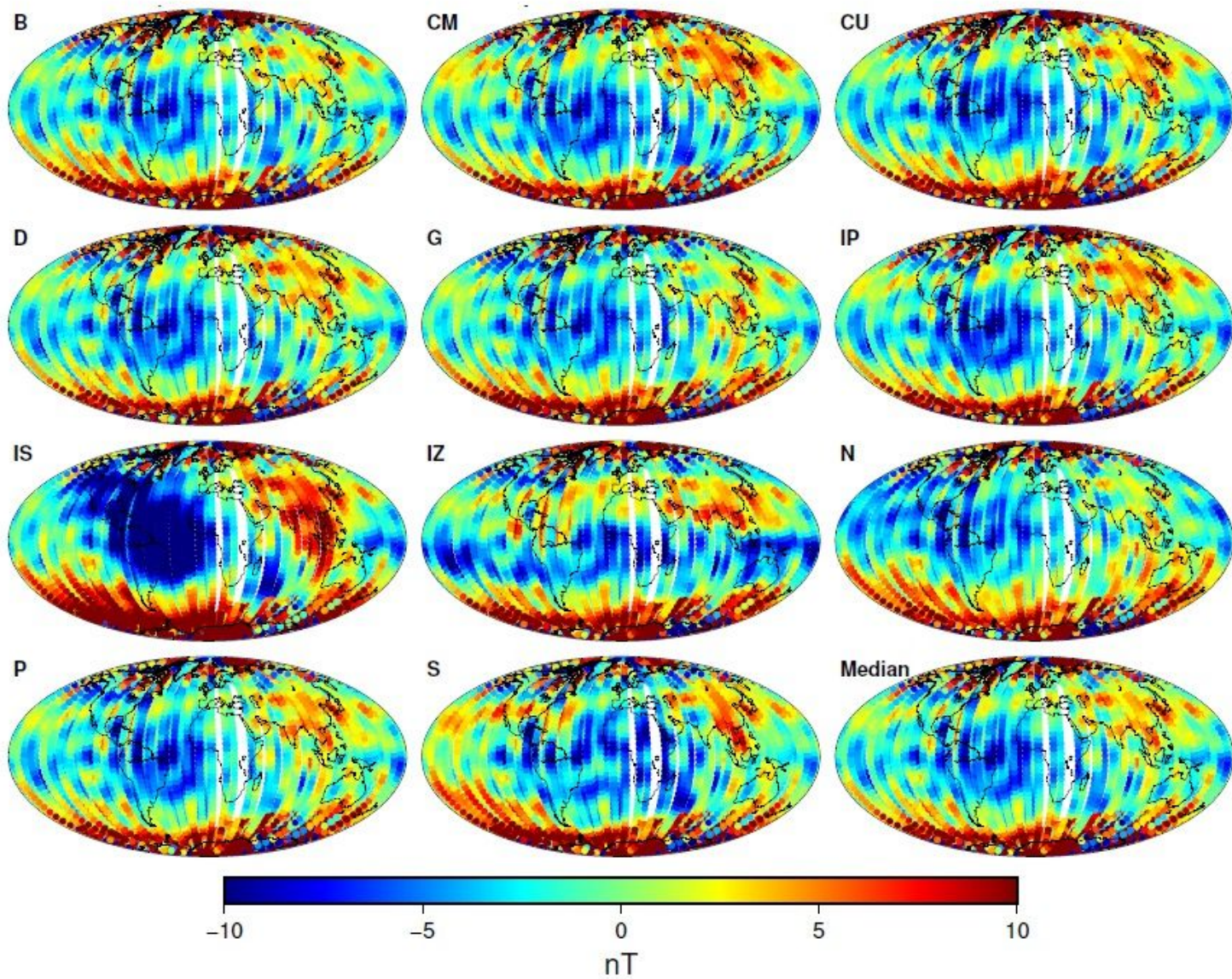


Figure 4

Vertical component (B_z) residuals between a combined Swarm A and B dataset and the DGRF-2015 candidates. The Swarm dataset spans 15 December 2014 to 15 January 2015.

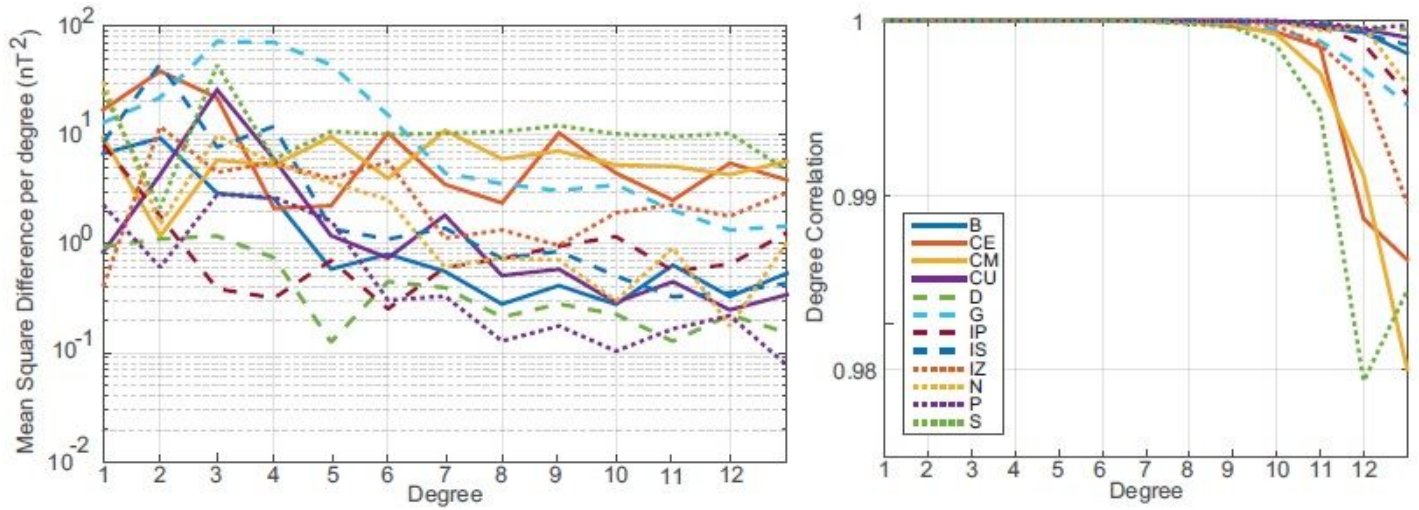


Figure 5

Power spectral differences (left) and degree correlation (right) between the IGRF-2020 candidates and the median model.

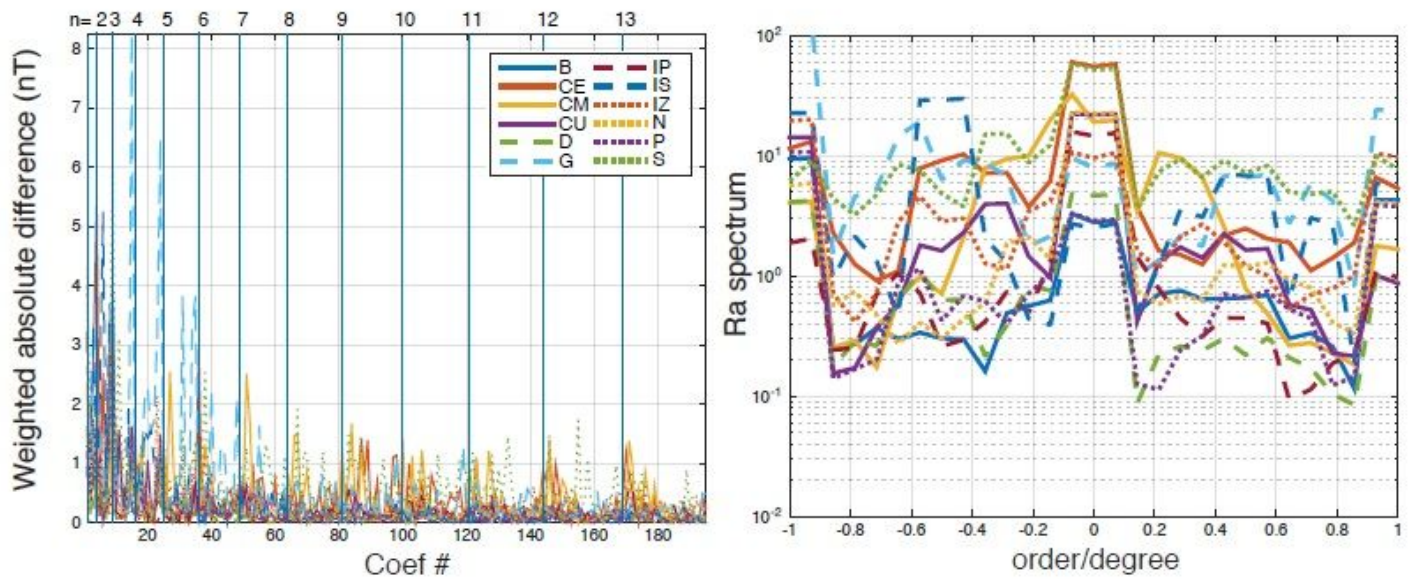


Figure 6

Absolute Gauss coefficient differences weighted by a factor of $p n + 1$ (left) and azimuthal power spectral differences (right) between the IGRF-2020 candidates and the median model.

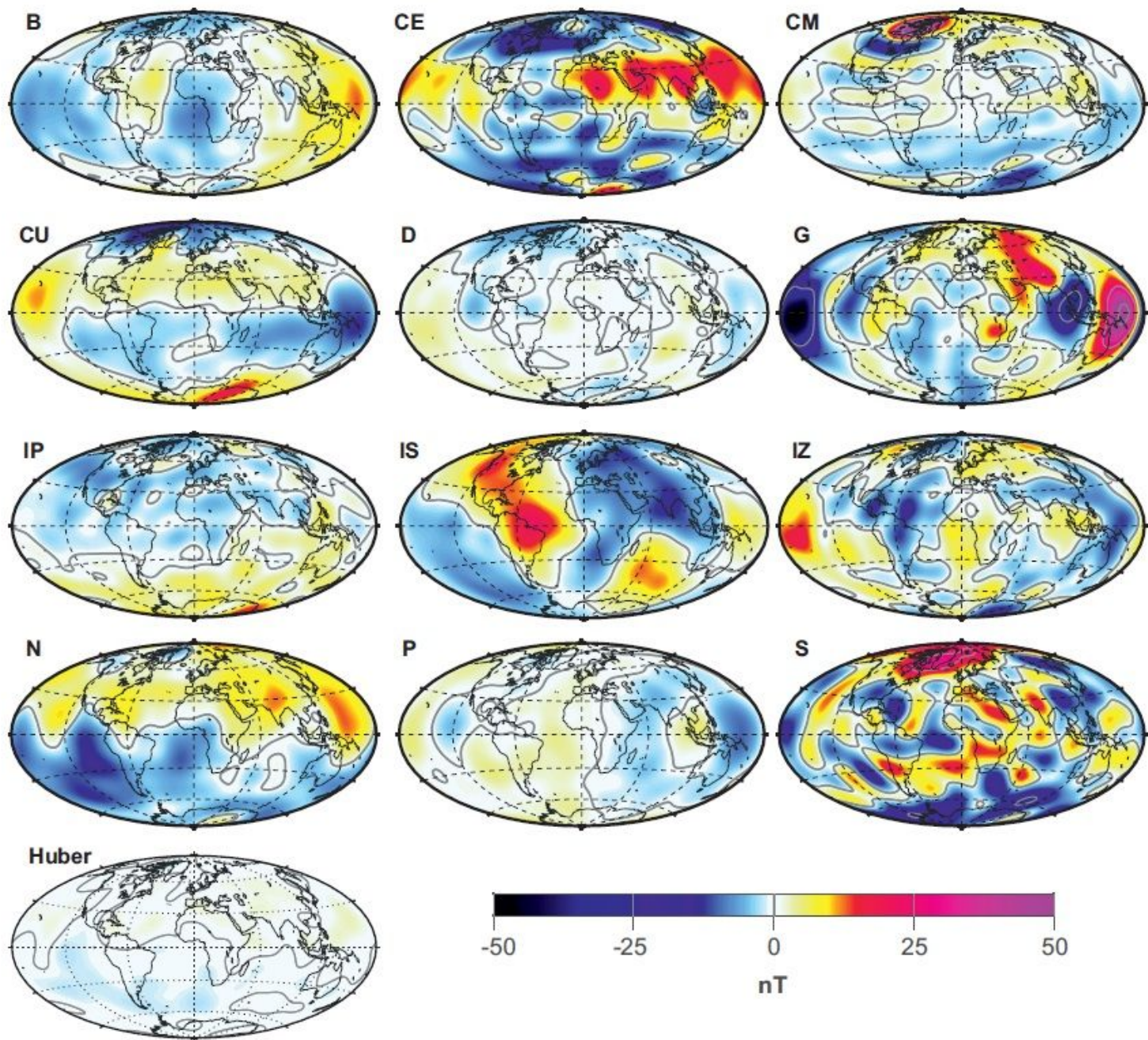


Figure 7

Differences (in nT) on the reference sphere $r = a$ between the vertical eld (B_z) of the IGRF-2020 candidates and the median model eld values at 2020.0

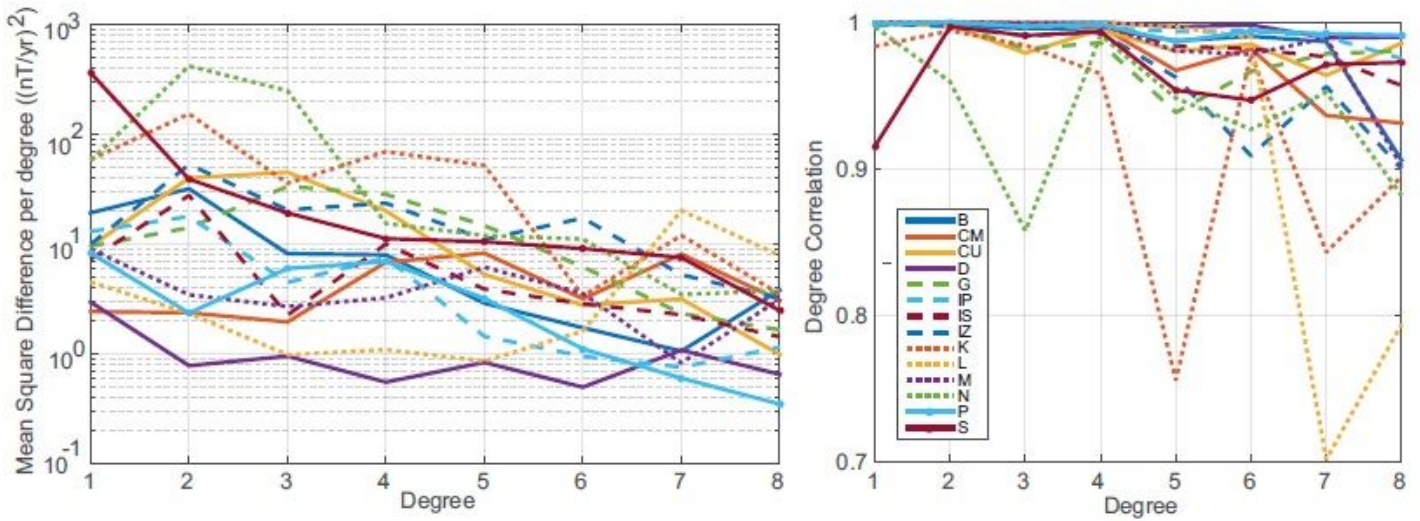


Figure 8

Power spectral differences (left) and degree correlation (right) between the SV-2020-2025 candidates and the robust model.

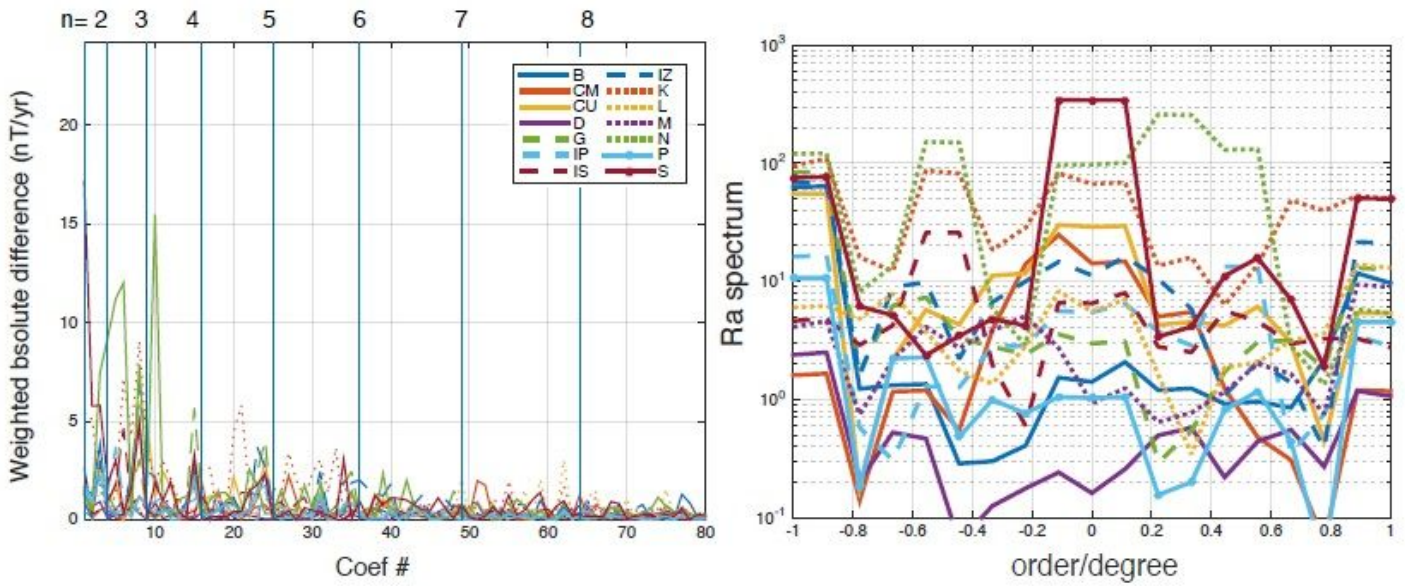


Figure 9

Absolute Gauss coefficient differences weighted by a factor of $p n + 1$ (left) and azimuthal power spectrum difference (right) between the SV-2020-2025 candidates and the robust model.

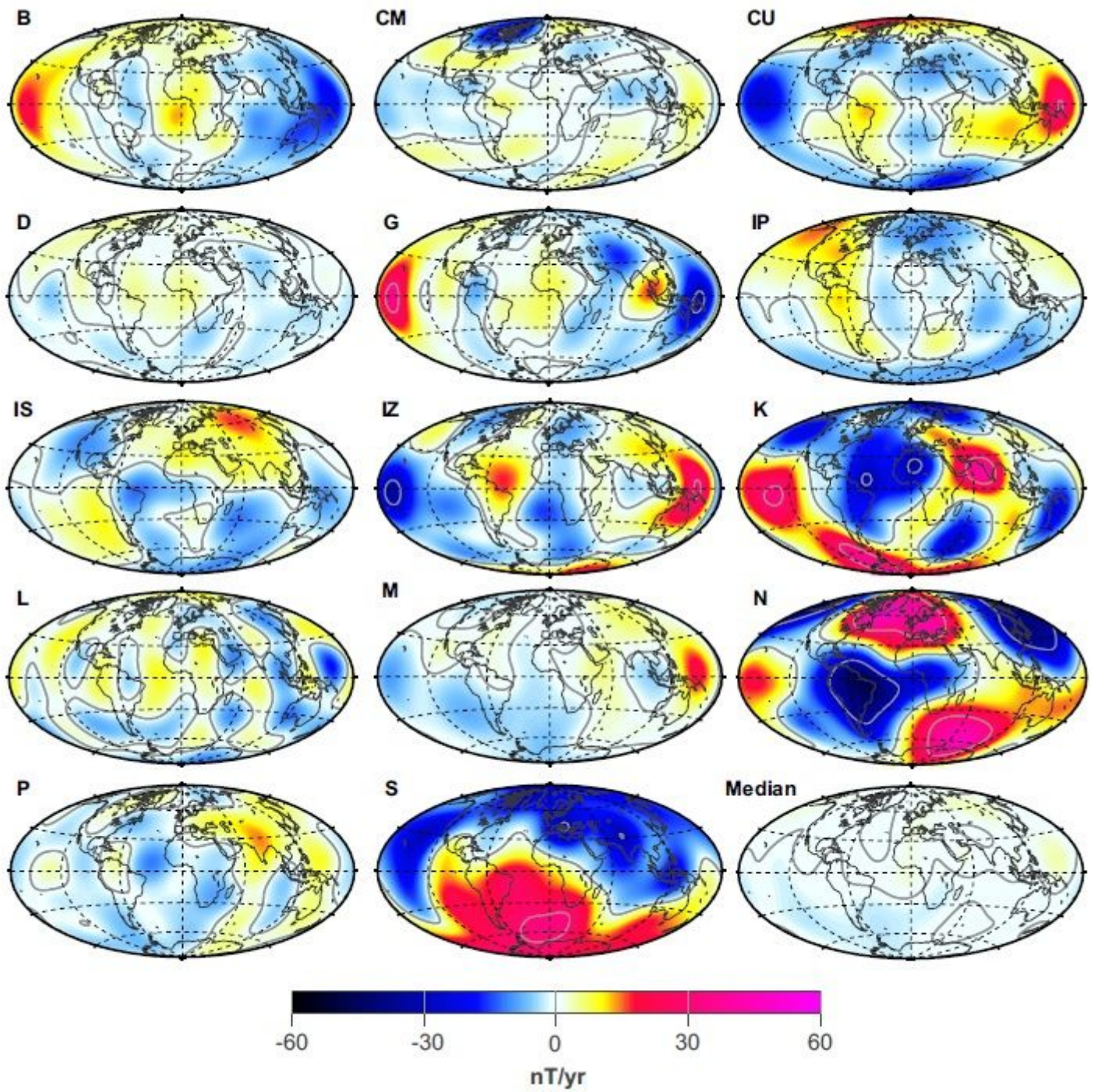


Figure 10

Annual average differences (in nT/yr) on the reference sphere $r = a$ between the vertical eld (dBz=dt) of the SV-2020-2025 candidates and the robust Huber model over 2020.0 to 2025.0.

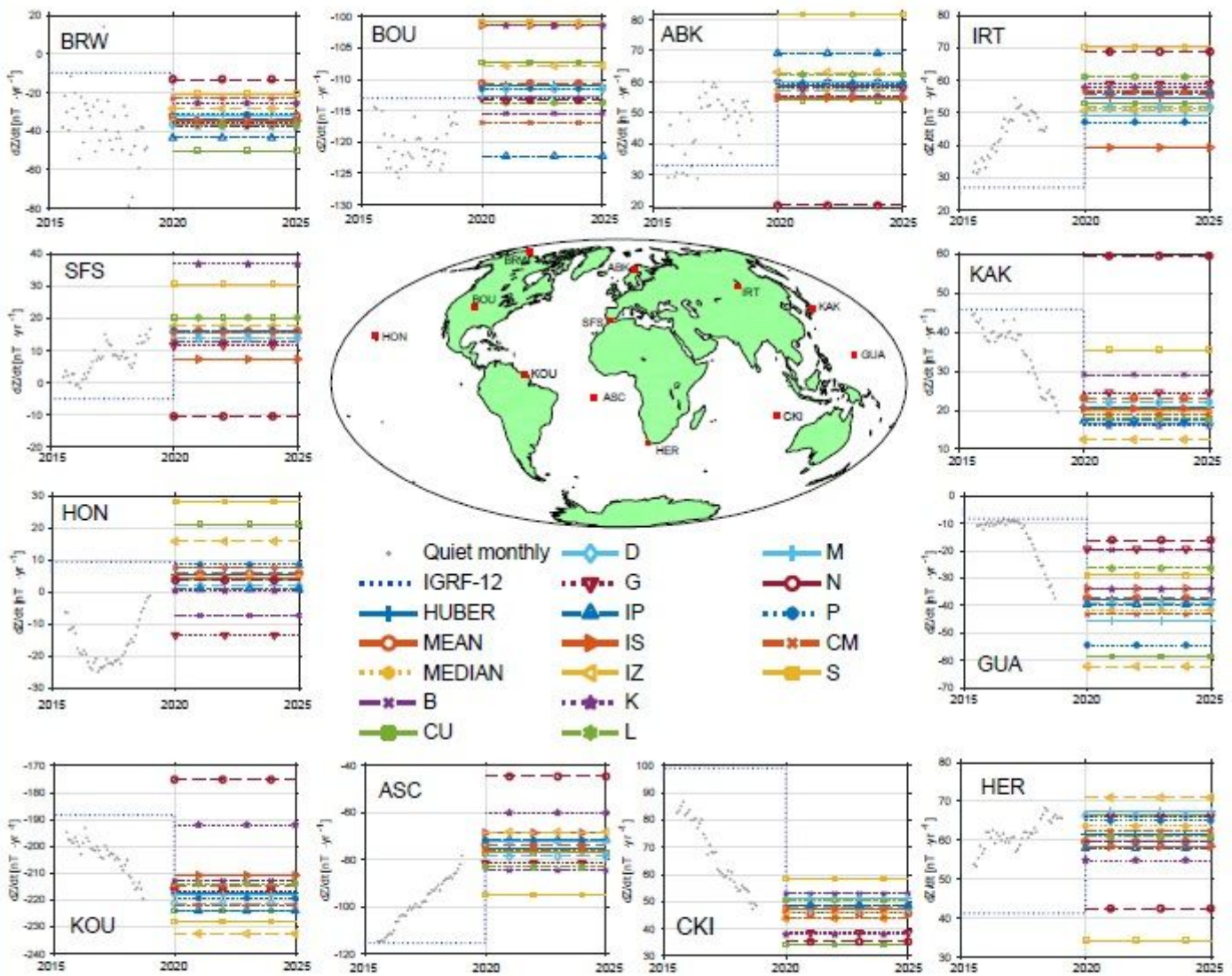


Figure 11

Comparison of the $dBz=dt$ component (NEC frame) of the IGRF-13 SV-2020-2025 candidates to selected observatory time-series over the 2015 to 2020 interval. The 2015{2020 SV values are from the IGRF-12 prediction.

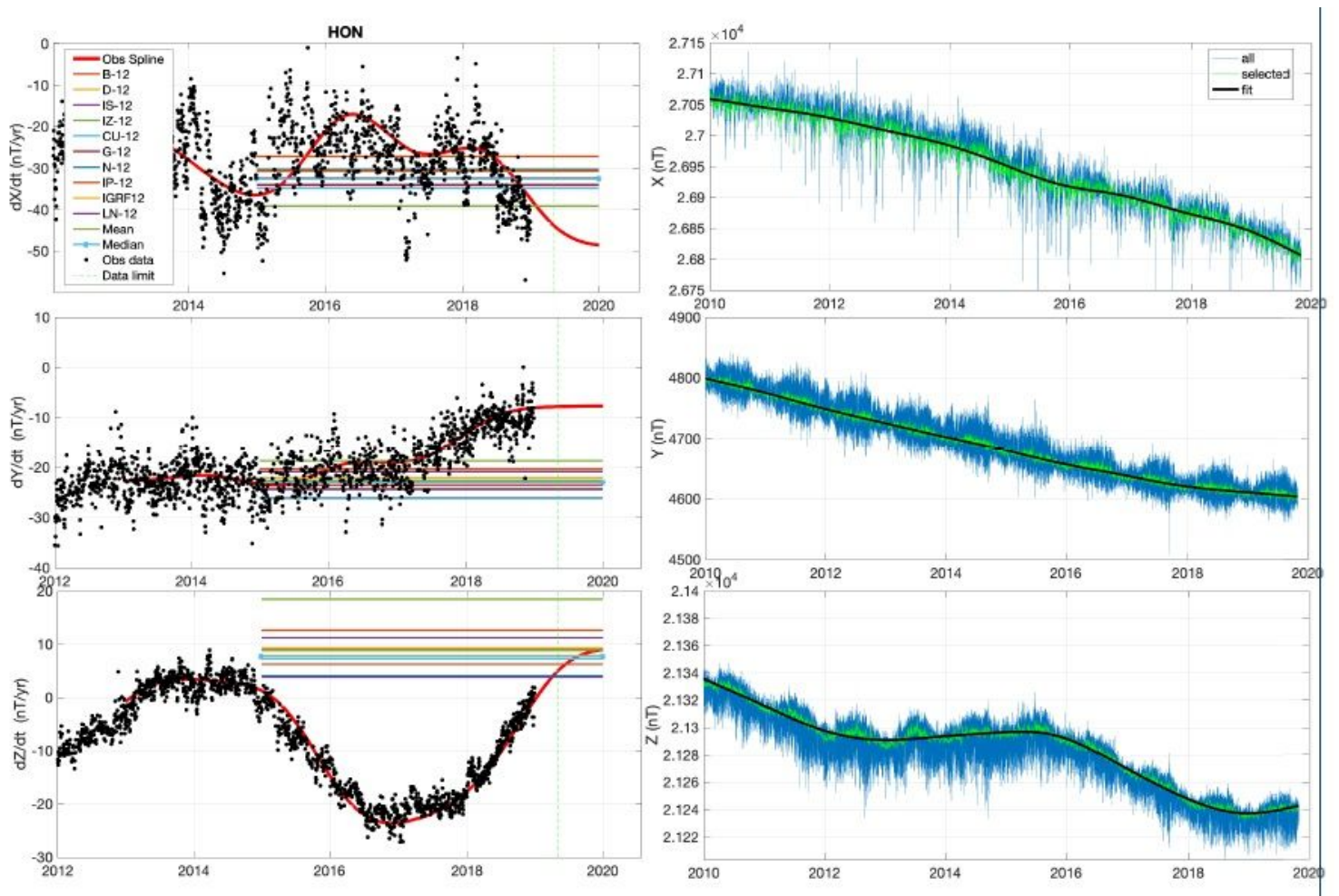


Figure 12

IGRF12 retroactive SV comparison at Honolulu (HON). Left panels show the observatory annual differences of daily mean values (black), annual spline difference curve (red) and IGRF12 candidate predictions for the $dB_x=dt$ (top), $dB_y=dt$ (middle), and $dB_z=dt$ (bottom) components in the NEC frame. Right panels show the original observatory data (blue), data after selecting for geomagnetically quiet periods (green), and tted spline curve (black) for the Bx (top), By (middle) and Bz (bottom) components.

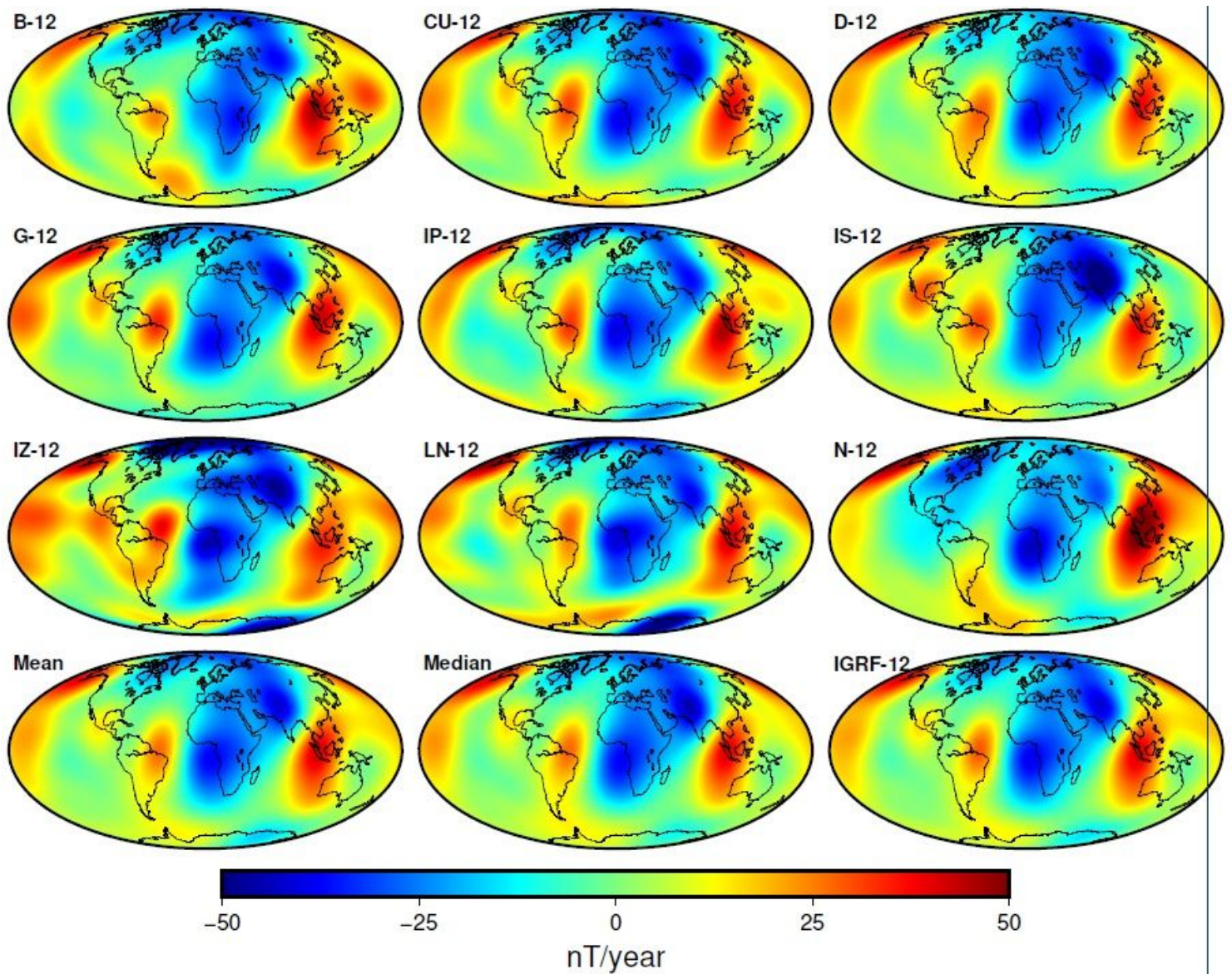


Figure 13

Spatial map differences of $\text{dBz}=\text{dt}$ (in nT/year) between IGRF-12 secular variation candidates and the IGRF-13 secular variation model over the 2015.0 to 2020.0 time period. We additionally include spatial map differences (against IGRF-13) of the mean and median of all IGRF-12 candidates, as well as the IGRF-12 SV model in the bottom row.

Supplementary Files

This is a list of supplementary files associated with this preprint. Click to download.

- [GraphicAbstract.jpg](#)